An iterative algorithm for predicting seafloor topography from gravity anomalies

Jinhai Yu[1], Bang An[1*], Huan Xu[1*], Zhongmiao Sun[2], Yuwei Tian[1], Qiuyu Wang[1]

[1]Key laboratory of computational Geodynamics, College of Earth and Planetary Sciences, University of Chinese Academy of Sciences, Beijing 100049, China

[2]National Key Laboratory of Geoinformation Engineering, Xi'an, 710054, China

Corresponding author: Bang An (anbang19@mails.ucas.ac.cn) and Huan Xu (xuhuan@ucas.ac.cn)

Key Points:

- An iterative algorithm to predict seafloor topography from gravity anomalies is theoretically established. Its validity is then verified by numerical simulations and application in predicting actual seafloor topography.
- Regarding the gravity anomalies, most of its low frequency parts are unrelated to the local seafloor topography. We proposed an efficient approach to remove that part of gravity anomalies.

Abstract

As high-resolution global coverage cannot easily be achieved by direct bathymetry, the use of gravity data is an alternative method to predict seafloor topography. Currently, the commonly used algorithms for predicting seafloor topography are mainly based on the approximate linear relationship between topography and gravity anomaly. In actual application, it is also necessary to process the corresponding data according to some empirical methods, which can cause uncertainty

in predicting topography. In this paper, we established analytical observation equations between the gravity anomaly and topography, and obtained the corresponding iterative solving method based on the least square method after linearizing the equations. Furthermore, the regularization method and piecewise bilinear interpolation function are introduced into the observation equations to effectively suppress the high-frequency effect of the boundary sea region and the low-frequency effect of the far sea region. Finally, the seafloor topography beneath a sea region (117.25°-118.25° E, 13.85°-14.85° N) in the South China Sea is predicted as an actual application, where gravity anomaly data of the study area with a resolution of 1′×1′ is from the DTU17 model. Comparing the prediction results with the data of ship soundings from the National Geophysical Data Center (NGDC), the root-mean-square (RMS) error and relative error can be up to 127.4 m and approximately 3.4%, respectively.

Plain Language Summary

The size of submarine mass and its distance from sea level affects gravity on it, which can make a difference in the gravity observed on sea level. We cut submarine mass into rectangular prisms one by one, establish and solve the equations between gravity and the height of each cuboid, and splice each cuboid to obtain topography of submarine mass at last. However, since there are some errors in gravity data, it is necessary to analyze their sources and propose algorithms to weaken their influence in order to improve the prediction accuracy of seafloor topography.

1 Introduction

As a natural density interface of the earth, the seafloor topography plays an important role in many geoscience fields (**Baudry and Calmant, 1996; Becker et al., 2009; Hsiao et al., 2011; Sandwell et al., 2006; Jekeli, 2017; Abulaitijiang et al., 2019**). Apart from the direct

measurement of sea depth by single/multi-beam technology, remote sensing technology and marine gravity data are also important for the indirect measurement of sea depth **(Lyzenga, 1978; Stumpf et al., 1985; Caballero and Richard, 2020**). For multi-beam echosounder, although it has a high accuracy, the distribution of actual ship soundings data is very sparse due to large time consumption and high cost (**Sanwell and Smith, 1997**). For remote sensing technology, the satellites including Sentinel-2, ICEsat, and others can measure the depth of shallow seas near islands and reefs with an accuracy of less than 1 m. However, depth prediction by remote sensing technology is limited as it can only capture the topographic features of sea areas with depths less than 18 m (**Rasheed et al., 2021**). Compared with multi-beam echosounder and remote sensing technology, marine gravity data is well distributed on the ocean. For example, geoid heights with a resolution better than 2 km can be obtained by integrating data of many altimetry satellites such as T/X satellite, Jason satellite, and Cryosat satellite, etc. (**Sandwell et al., 2014**), from which gravity data, such as the gravity anomaly and gravity gradients, can be satisfactorily computed (**Andersen, 2020; Yu D C et al., 2021**). Therefore, a highly effective method for mapping seafloor topography is as follows: first, gravity data with a high resolution (e.g., 2 km) can be used to predict seafloor topography with the same resolution, and the data of sea depths from ship soundings and remote sensing can then be combined to refine the topography. In fact, using gravity anomaly to predict seafloor topography can effectively fill the lack of ship sounding data and improve the overall accuracy of the seafloor topography.

Considering the research status quo of using gravity data to predict seafloor topography, gravity anomaly has been used as the main type of data (**Calmant, 1994; Smith and Sandwell, 1997; Kim et al., 2011)**. Additionally, vertical gravity gradient data have also been used to a lesser extent (**Hu et al., 2014; Kim and Wessel, 2016; Yang et al., 2018; Xu and Yu, 2022**). The

prediction methods are mainly divided into the spatial and frequency-domain methods. A typical representative of the spatial method is the gravity-geologic method (GGM) based on the Bouguer correction formula; namely, the relationship between the gravity generated by an infinite uniform thick plate and the height of the thick plate is linear; thus, the relationship between the gravity anomaly and seafloor topography can be fitted by existing ship soundings (**Imbrahim and Hinze, 1972; Hwang, 1999; Kim et al., 2011**). Essentially, GGM is a fitting method that can be easily computed, but it cannot predict heavily undulating seafloor topography (**Yang et al., 2018**). The frequency-domain method for predict seafloor topography is based on the Parker formula (**Parker, 1972**) that essentially is a first-order approximate formula omitting the high-order terms of sea depth. The frequency-domain method needs to consider the flexural isostatic compensation theory to improve its accuracy; thus, more geophysical parameters are required (**Dixon et al., 1983; Baudry et al., 1987**).

Parker formula can be summarized as follows. For a local sea surface, it can be approximated as the $O-xy$ plane. If z-axis is downward, then the spatial coordinate is $O-xyz$. Assuming that $R=\{(x,y);\ -a\le x\le a,-b\le y\le b\}$ is a region on the sea surface, $h(x,y)$ is the sea depth at (x,y) on sea surface, and $\Omega=\{(x,y,z);\ (x,y)\in R,0\le z\le h(x,y)\}$ is a curved column of seawater with density ρ_w below R; the gravitational potential generated by Ω at $(x,y)\in R$ is then expressed as:

$$v_R(x,y)=\mathrm{G}\rho_w\iiint_{\Omega}\frac{1}{\sqrt{(\xi-x)^2+(\eta-y)^2+\zeta^2}}\mathrm{d}\xi\mathrm{d}\eta\mathrm{d}\zeta \tag{1}$$

where G is the Newton gravitational constant. Using **Eq. (1)** and omitting high-order quantities of $h(x,y)$, **Parker (1972)** derived a linear relationship between Fourier transforms of $v_R(x,y)$ and $h(x,y)$; namely, the relationship between $v_R(x,y)$ and $h(x,y)$ in the frequency domain.

Considering that $g_R(x,y)$ is the gravity corresponding to $v_R(x,y)$, the relationship between $g_R(x,y)$ and $h(x,y)$ in the frequency domain can also be deduced (**Jekeli, 2017; Zhu, 2007**).

Although the Parker formula has been widely used in predicting seafloor topography, the omitted second-order quantity $O(f \cdot h^2)$ still has a large impact for high frequencies (large f) and large sea depth *h*, where $f = \sqrt{f_1^2 + f_2^2}$ and (f_1, f_2) are frequency-domain variables. **Yang et al. (2018)** has pointed out that the Parker formula is less accurate in sea areas with large variations in the seafloor topography.

The purpose of this paper is to directly compute the gravity $g_R(x,y)$ generated by Ω to establish a rigorous set of observation equations between the gravity anomaly and sea depth $h(x,y)$. Subsequently, the solvability and anti-error property of the observation equations are investigated by numerical simulation. Simultaneously, the spectral characteristics of the measured gravity anomaly are also analyzed to eliminate disturbances in the gravity anomaly and predict seafloor topography accurately. Finally, to verify effectiveness of our algorithm, a sea region in the South China Sea is selected as a test area to predict its seafloor topography.

2 Theory and methods

2.1 Computational formula of gravity

The mathematical expression for the vertical gravity generated by a rectangular prism of constant density is introduced here (**Nagy, 1966; Blakely, 1995; Nagy et al., 2000**). We assumed that $A = \{(\xi,\eta,\zeta);\ x_1 \le \xi \le x_2, y_1 \le \eta \le y_2, z_1 \le \zeta \le z_2\}$ is a rectangular prism of constant density ρ_A and $Q(x_Q, y_Q, z_Q)$ is any point outside *A*. Introducing the notations

$$\begin{cases} \xi_1 = x_1 - x_Q, \quad \xi_2 = x_2 - x_Q \\ \eta_1 = y_1 - y_Q, \quad \eta_2 = y_2 - y_Q \\ \zeta_1 = z_1 - z_Q, \quad \zeta_2 = z_2 - z_Q \end{cases} \tag{2}$$

and

$$r = \sqrt{(\xi - x_Q)^2 + (\eta - y_Q)^2 + (\zeta - z_Q)^2} \tag{3}$$

then the vertical gravity at point Q generated by A is

$$\begin{aligned} g_A(x_Q, y_Q, z_Q) &= \mathrm{G}\rho_A \iiint_A \frac{\zeta - z_Q}{\sqrt{[(\xi - x_Q)^2 + (\eta - y_Q)^2 + (\zeta - z_Q)^2]^3}} \mathrm{d}\xi \mathrm{d}\eta \mathrm{d}\zeta \\ &= \mathrm{G}\rho_A \left[\left\| \xi \ln(\eta + r) + \eta \ln(\xi + r) - \zeta \arctan \frac{\xi\eta}{\zeta r} \right|_{\xi_1}^{\xi_2} \Big|_{\eta_1}^{\eta_2} \Big|_{\zeta_1}^{\zeta_2} \right] \end{aligned} \tag{4}$$

where the vertical gravity represents the derivation of the gravitational potential with respect to the variable z.

If $z_1 = 0$ in the rectangular prism A and $z_Q = 0$, assuming that $R = \{(x, y);\ x_1 \le x \le x_2, y_1 \le y \le y_2\}$ is the rectangular region corresponding to the rectangular prism A on the sea surface (refer to **Fig. 3a**), then **Eq. (4)** can be simplified as

$$g_A(x_Q, y_Q, 0) = \mathrm{G}\rho_A \cdot J_R(x_Q, y_Q, z_2) \tag{5}$$

where z_2 is the sea depth of A, and

$$J_R(x_Q, y_Q, z_2) = \left\| \xi \ln \frac{\eta + \sqrt{\xi^2 + \eta^2 + z_2^2}}{\eta + \sqrt{\xi^2 + \eta^2}} + \eta \ln \frac{\xi + \sqrt{\xi^2 + \eta^2 + z_2^2}}{\xi + \sqrt{\xi^2 + \eta^2}} - z_2 \arctan \frac{\xi\eta}{z_2 \sqrt{\xi^2 + \eta^2 + z_2^2}} \right|_{\xi_1}^{\xi_2} \Big|_{\eta_1}^{\eta_2} \tag{6}$$

Notably, (x_Q, y_Q) in **Eqs. (5)** and **(6)** can assume the range of whole local sea surface $O-xy$. Therefore, **Eqs. (5)** and **(6)** are analytical formulas for the gravity on the sea surface generated by the rectangular prism $A=\{(\xi,\eta,\zeta);\ x_1\le\xi\le x_2, y_1\le\eta\le y_2, 0\le\zeta\le z_2\}$ below the sea surface. The derivation details and expression form can refer to the work of **Nagy et al (2000).**

2.2 Establishing the observation equations for sea depth from the gravity anomaly

In the following, the local coordinate system $O-xyz$ can be established by considering the local sea surface as $O-xy$ and the *z*-axis downward (away from the sea surface). Assuming that $R=\{(x,y);\ -a\le x\le a, -a\le y\le a\}$ is a square area on the sea surface (called the target area), $h(x,y)$ is the sea depth at (x,y) (to be solved), and $\Omega=\{(x,y,z);\ (x,y)\in R,\ 0\le z\le h(x,y)\}$ is the curved column formed by the region of seawater below *R*. If seawater in Ω is replaced by rocks beneath seafloor, then the gravity anomaly at point $Q(x_Q,y_Q)$ on *R* generated by Ω is

$$\delta g_R(x_Q,y_Q)=\mathrm{G}\Delta\rho\iiint_{\Omega}\frac{\zeta}{\sqrt{[(\xi-x_Q)^2+(\eta-y_Q)^2+\zeta^2]^3}}\mathrm{d}\xi\mathrm{d}\eta\mathrm{d}\zeta \tag{7}$$

where $\Delta\rho=\rho_w-\rho_c$, and ρ_c and ρ_w are the average densities of the lithosphere and seawater respectively. Assuming that *t* is the step length, and (x_i,y_j) is the partition points of *R*, wherein $x_i=i\cdot t$, $y_j=j\cdot t$, and $a=N\cdot t$. If the length *t* is small, the curved column below the segmented subdomain $R_{ij}=[x_i,x_{i+1}]\times[y_j,y_{j+1}]$ of *R* can then be approximated as a prism $\Omega_{ij}=\{x_i\le x\le x_{i+1}, y_j\le y\le y_{j+1}, 0\le z\le h_{ij}\}$, where h_{ij} is the average depth of $[x_i,x_{i+1}]\times[y_j,y_{j+1}]$. Using **Eq. (5)**, **Eq. (7)** can be expressed as

$$\delta g_R(x_Q,y_Q)=\mathrm{G}\cdot\Delta\rho\sum_{i,j=-N}^{N-1}J_{R_{ij}}(x_Q,y_Q,h_{ij}) \tag{8}$$

where $J_{R_{ij}}$ is computed by Eq. (6). If the gravity anomaly $\delta g_R(x_Q, y_Q)$ on R is obtained in advance, then **Eq. (8)** is the set of observation equations for sea depth h_{ij}.

Variations of the gravity anomaly on the sea surface are mainly caused by the mass deficit by the seafloor topography, density anomaly of the lithosphere, and isostatic compensation of mass below the lithosphere. The mass deficit by seafloor topography significantly contributes to the gravity anomaly on the sea surface, whereas the contributions of other factors are smoothed by upward continuation (**Fan et al., 2021**).

In terms of the magnitudes of the influences, the closer the distance to R, the larger the influence on the gravity anomaly on R. In the following **Fig. 1**, the regions that have an effect on the gravity anomaly on R are divided into the boundary, far, and deep regions, and the methods to deal with these effects are investigated individually.

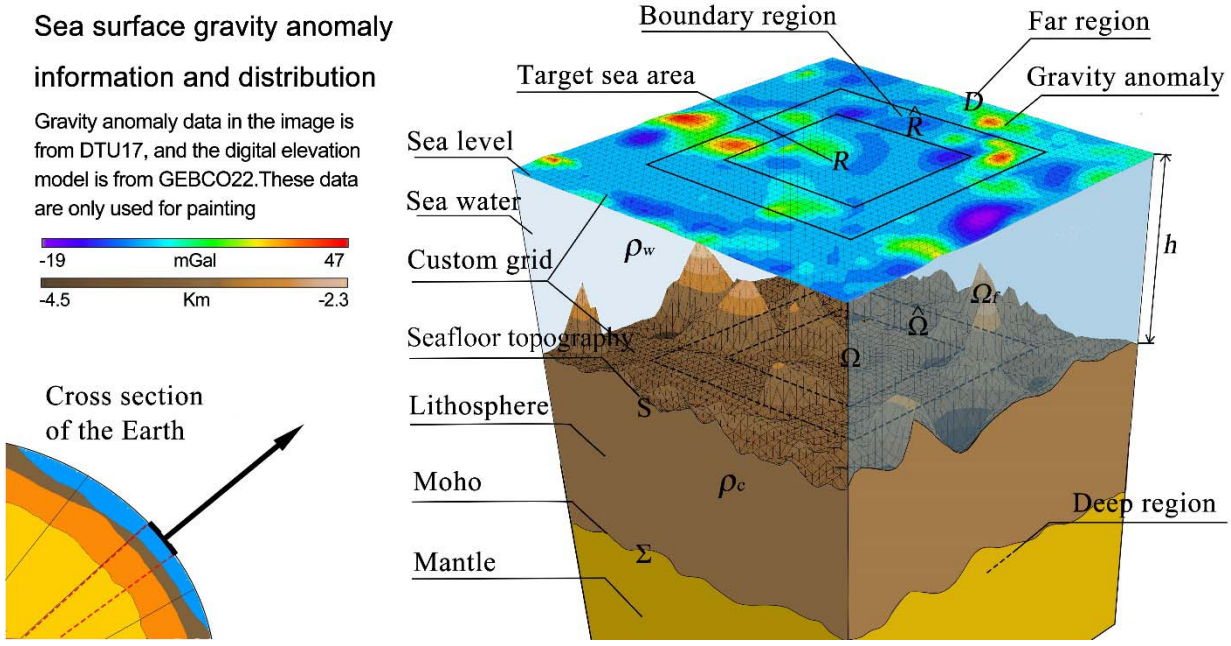

Figure 1. Information and distribution of the gravity anomaly on the sea surface, where Σ and S represent the Moho surface and seafloor topography, respectively; R, $\hat{R}$ and D represent the

corresponding target, boundary and far regions on the sea surface, respectively; ρ_{w} and ρ_{c} represent the densities of seawater and bedrock, respectively.

2.2.1 Observation equations by considering the boundary region

By extending *R* outside the boundary by *M* steps, $\hat{R}=\{(x,y);\ -(M+N)t\le x,y\le(M+N)t\}$ is introduced. Subsequently, $\hat{R}-R$ is called the boundary region of *R*, and the effect of its topography on solving the sea depth below *R* is called the boundary effect. By considering the boundary effect, **Eq. (8)** can be written as

$$\mathrm{G}\Delta\rho\sum_{i,j=-(N+M)}^{N+M-1}J_{R_{ij}}(x_Q,y_Q,h_{ij})=\delta g_{\hat{R}}(x_Q,y_Q),\quad (x_Q,y_Q)\in R \tag{9}$$

where $\delta g_{\hat{R}}(x_Q,y_Q)$ is the gravity anomaly generated by the curved column $\hat{\Omega}$ formed by the seawater below $\hat{R}$. **Eq. (9)** is the system of observation equations for sea depth h_{ij} below *R* after considering the boundary effect.

We then subdivided the grid points on *R*, namely, we consider $(\hat{x}_p,\hat{y}_q)\in R$, where $\hat{x}_p=\frac{pt}{2}$, $\hat{x}_p=\frac{pt}{2}$, and $p,q=0,\pm1,\cdots,\pm2N$. If the gravity anomaly $\delta g_{\hat{R}}(\hat{x}_p,\hat{y}_q)$ is known, the following equation is obtained

$$\mathrm{G}\Delta\rho\sum_{i,j=-(N+M)}^{N+M-1}J_{R_{ij}}(\hat{x}_p,\hat{y}_q,h_{ij})=\delta g_{\hat{R}}(\hat{x}_p,\hat{y}_q) \tag{10}$$

where $p,q=0,\pm1,\cdots,\pm2N$. Notably, the number of equations in **Eq. (10)** is $(4N+1)^2$ and the number of unknowns is $(2N+2M)^2$; thus, $N\ge M$ is required to ensure that **Eq. (10)** has enough

equations. As **Eq. (10)** is nonlinear with respect to the solved variables h_{ij}, linearization must be conducted. After linearization, the corresponding iterative procedure for h_{ij} is

$$\mathrm{G}\Delta\rho \sum_{i,j=-(N+M)}^{N+M-1} \frac{\partial J_{R_{ij}}(\hat{x}_p, \hat{y}_q, h_{ij}^{(k)})}{\partial h_{ij}^{(k)}} [h_{ij}^{(k+1)} - h_{ij}^{(k)}] = \delta g_{\hat{R}}(\hat{x}_p, \hat{y}_q) - \mathrm{G}\Delta\rho \sum_{i,j=-(N+M)}^{N+M-1} J_{R_{ij}}(\hat{x}_p, \hat{y}_q, h_{ij}^{(k)}) \tag{11}$$

where $k = 0,1,\cdots$, and $h_{ij}^{(0)}$ is the iterative initial value of h_{ij}.

2.2.2 Effect of the deep region: correction for the Moho undulation

Fig. 1 shows that the effect of the deep region of Earth on the gravity anomaly on *R* is mainly derived from the undulation of the Moho surface; hereafter, this effect is simply called the "deep effect." In physical geodesy, Venning-Meinesz or the Airy isostatic theory is usually used to determine the Moho surface. In this paper, the Airy isostatic theory is recommended. Notably, for a seamount with depth *h*, if ρ_w, ρ_c and ρ_m are the densities of seawater, lithosphere, and upper mantle, respectively, and *L* is the height of the Moho surface uplift corresponding to the seamount, then $L = \frac{\rho_c - \rho_w}{\rho_m - \rho_c} h$ and $T_0 - L$ represent the depth of the Moho surface from the sea surface below the seamount (**Heiskanen and Moritz, 1967; Calment and Baudry, 1996)**, where $T_0 = 25$ km is usually chosen.

According to the Airy isostatic theory, the depth $T_0 - L$ of the Moho surface can directly be derived from the depth *h* of the seamount. As the depth of the Moho surface from sea surface is much larger than the depth *h* of the seamount, the effect of the Moho surface undulation on the gravity anomaly can easily be reduced with the help of the Airy isostatic theory after the seafloor topography is preliminarily solved. Therefore, the deep effect, such as the Moho surface undulation, can be corrected in advance.

2.2.3 System of observation equations in the general case

If the target area R is extended to whole sea surface S in **Eq. (8)**, and the gravity anomaly generated by the density difference of seawater with respect to the lithosphere is $\delta_S g$, then considering $(x,y)\in R$, we have

$$\mathrm{G}\Delta\rho \sum_{i,j=-(N+M)}^{N+M-1} J_{R_{ij}}(x,y,h_{ij}) = \delta g_S(x,y) - \delta g_D(x,y) \tag{12}$$

where D is the far region (**Fig. 1**) and $\delta_D g$ is the gravity anomaly generated by the density difference of seawater with respect to the lithosphere below D. Notably, $\delta_D g$ is the effect of the far region on the gravity anomaly and is simply called the far effect hereafter.

Generally, assuming that v is the Earth's gravitational potential and v_S is the gravitational potential generated by replacing seawater in the ocean with the rock in the lithosphere, we obtain $\delta g_S = \frac{\partial(v - v_S)}{\partial z}$ on R. If V is the Somigliana gravitational potential and $T = v - V$ is the disturbing potential, we obtain the following on R

$$\frac{\partial T}{\partial z} = \delta g_S + \frac{\partial(v_S - V)}{\partial z} \tag{13}$$

If the isostatic theory is used to eliminate the effect of the Moho surface, then the deep effect $\frac{\partial(v_S - V)}{\partial z}$ exhibits characteristics of long waves on the sea surface according to the circle construction of Earth density (i.e., Earth density is distributed in a laminar pattern). Substituting **Eq. (13)** into **Eq. (12)**, then at $(x,y)\in R$, we have

$$\mathrm{G}\Delta\rho \sum_{i,j=-(N+M)}^{N+M-1} J_{R_{ij}}(x,y,h_{ij}) = \frac{\partial T(x,y)}{\partial z} - \delta g_D(x,y) - \frac{\partial(v_S - V)}{\partial z} \tag{14}$$

198 As the coordinate system *O-xyz* is locally established near *R*, $\frac{\partial T}{\partial z} = -\frac{\partial T}{\partial r} = \delta g$ on *R*, where

199 δg is the gravity anomaly based on the Somigliana gravity field, whose data can be obtained by

200 the known gravity field models, such as EGM2008 or DTU17. Assuming that

201 $F(x,y) = -\delta g_D(x,y) - \frac{\partial (v_S - V)}{\partial z}$, then at $(x,y) \in R$, we have

$$\mathrm{G}\Delta\rho \sum_{i,j=-(N+M)}^{N+M-1} J_{\Omega_{ij}}(x,y,h_{ij}) = \delta g(x,y) + F(x,y) \tag{15}$$

202 where $F(x,y)$ is the long wave (or low frequency) on *R* and is continuous. If the values of

203 $F_{ij} = F(x_i, y_j)$ at partition points of *R* are known, then a bilinear interpolation function $\hat{F}_{ij}(x,y)$

204 can be obtained using the function values F_{ij}, $F_{i+1,j}$, $F_{i,j+1}$, and $F_{i+1,j+1}$ on each sub rectangle of

205 R_{ij}. In general, for any $(x,y) \in R$, we assumed that $\hat{F}(x,y,\mathbf{F}) = \hat{F}_{ij}(x,y)$, where $(x,y) \in R_{ij}$, and **F**

206 is the vector comprising values F_{ij} at all partition points. Notably, $\hat{F}(x,y,\mathbf{F})$ is continuous on *R*

207 with respect to (x,y) and linear with respect to **F**. Moreover, $\hat{F}(x,y,\mathbf{F})$ is the piecewise bilinear

208 interpolation function of $F(x,y)$. $F(x,y)$ is the long wave on *R* and its wavelength is much larger

209 than the step length *t* to partition *R*, so $\hat{F}(x,y,\mathbf{F}) \approx F(x,y)$. Thus, **Eq. (15)** can finally be expressed

210 as

$$\mathrm{G}\Delta\rho \sum_{i,j=-(N+M)}^{N+M-1} J_{\Omega_{ij}}(x,y,h_{ij}) = \delta g(x,y) + \hat{F}(x,y,\mathbf{F}), \quad (x,y) \in R \tag{16}$$

211 where h_{ij} and F_{ij} are the variables to be solved.

212 So far, we have established three sets of observation equations for predict sea depth h_{ij},

213 namely, **Eqs. (8)**, **(10)**, and **(16)**, where **Eq. (8)** is established by only considering the target region

214 R; **Eq. (10)** is established after considering the boundary effect of R; and **Eq. (16)** is established
215 after considering both the boundary effect of R and the far effect. As the observation equations are
216 nonlinear with respect to the sea depth h_{ij}, they should be linearized for h_{ij} in actual
217 computation. For example, **Eq. (11)** is the result of linearization of **Eq. (10)**. Additionally, **Eq.**
218 **(16)** is linear with respect to the variable **F**; thus, only the variable h_{ij} should be linearized in **Eq.**
219 **(16)**.

220 **2.3 Regularization method for the solving equations**

221 This paragraph mainly discusses the solvability problem for observation equations. To ensure
222 that the descriptions are clear, only **Eq. (11)** is discussed as an example. Introducing matrix

$$A_k = \mathrm{G}\Delta\rho\left(\frac{\partial J_{R_{ij}}(\hat{x}_p,\hat{y}_q,h_{ij}^{(k)})}{\partial h_{ij}^{(k)}}\right)_{pq,ij} \tag{17}$$

223 and vector

$$\mathbf{b}_k = \left[\delta g_{\hat{R}}(\hat{x}_p,\hat{y}_q) - \mathrm{G}\Delta\rho\sum_{i,j=-(N+M)}^{N+M-1} J_{\Omega_{ij}}(\hat{x}_p,\hat{y}_q,h_{ij}^{(k)})\right]_{pq} \tag{18}$$

224 and solving for vector $\mathbf{h}_k = \left[h_{ij}\right]_{ij}$, the iterative matrix form of **Eq. (11)** is expressed as

$$A_k\mathbf{h}_{k+1} = \mathbf{b}_k + A_k\mathbf{h}_k \tag{19}$$

225 As the known data $\delta g_{\hat{R}}(\hat{x}_p,\hat{y}_q)$ in **Eqs. (11)** or **(19)** are given only on R, and the sea depths h_{ij} to
226 be solved (where $i,j=-(N+M),\cdots,0,\cdots,N+M-1$) contain the sea depths of the boundary
227 region in addition to those of R, directly solving **Eq. (19)** may lead to poor solvability of the

system of equations. To ensure solvability, a regularization factor $\alpha > 0$ is introduced, namely, the actual solved system of equations is expressed as

$$(A_k^T A_k + \alpha E)\mathbf{h}_{k+1} = A_k^T (\mathbf{b}_k + A_k \mathbf{h}_k) \tag{20}$$

where E is the unit matrix. Notably, **Eq. (20)** has a unique solution $\mathbf{h}_{k+1}$ if $\mathbf{h}_k$ is known.

Notably, the sea depth below the boundary sea $\hat{R} - R$ is divergent when iteratively solving **Eq. (20)**. To ensure convergence of the iterative process, the sea depth below $\hat{R} - R$ is always considered as the average of the sea depth below R in each iteration. After this treatment, **Eq. (20)** can be solved iteratively. The flow construction of the analytical iterative algorithm is shown in **Fig. 2**.

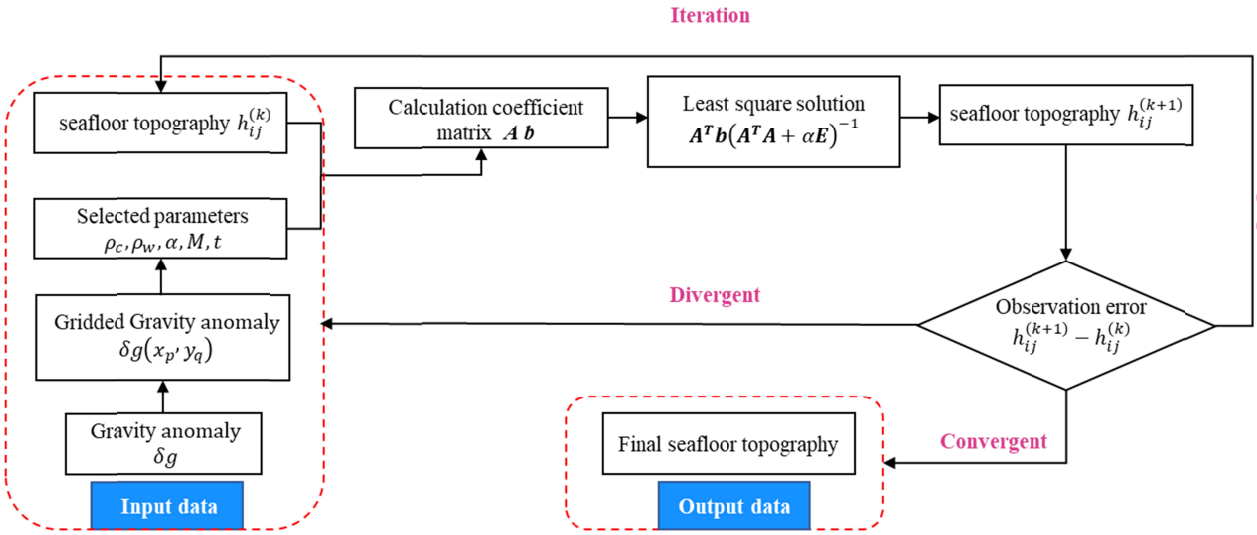

Figure 2. Flow chart of the iterative algorithm for the seafloor topography.

3 Simulation Experiment

3.1 Selection of some parameters

This section discusses the solvability of **Eq. (11)** or **(20)** by simulations, namely, by only considering the boundary effect. In this section, the bedrock and seawater densities are chosen as

ρ_c=2.7×10^{3}kg/m^3 and ρ_w=1.03×10^{3}kg/m^3, respectively, namely, $\Delta\rho = -1.67\times10^3$ kg/m^3. Notably, the smaller the step length of partition for the target region *R*, the higher is the accuracy of the solved sea depth beneath *R*. However, as the gravity anomaly on the sea surface in the actual calculation has a resolution of 1′×1′, the step length is always chosen as $t = 2$ km in simulation computations. Additionally, as the boundary effect is considered, the extension number *M* in $\hat{R}$ should be chosen carefully. According to discussions by Yu and Xu (2021), we choose that $M = 10$, namely, $\hat{R}$ is obtained by extending *R* outward for 20 km.

We then selected a sea area of 96 km×96 km in the South China Sea as $\hat{R}$; its internal sea area of 56×56 km is the target region *R*, and the seafloor topography beneath $\hat{R}$ is chosen from the GEBCO_22 bathymetric model. After gridding $\hat{R}$ by a step length of 2 km, the seafloor topography beneath $\hat{R}$ is shown in **Fig. 3a**. This implies that the number of partitions for *R* is $N = 14$. According to the GEBCO_22 model, the maximum undulation of the seafloor topography below *R* is 610.0 m. Subsequently, this seafloor topography is placed at sea depth *H* below $\hat{R}$, and the gravity anomaly $\delta g_{\hat{R}}$ generated by it can then be computed. **Fig. 3b** shows the distribution of $\delta g_{\hat{R}}$ on $\hat{R}$ where $H = 6$ km. We aimed to solve the seafloor topography beneath *R* from $\delta g_{\hat{R}}$ on *R* using **Eq. (11)** or **(20)**, and then compare it with the "real seafloor topography" beneath *R*. Notably, *H* is the maximum sea depth of the seafloor topography.

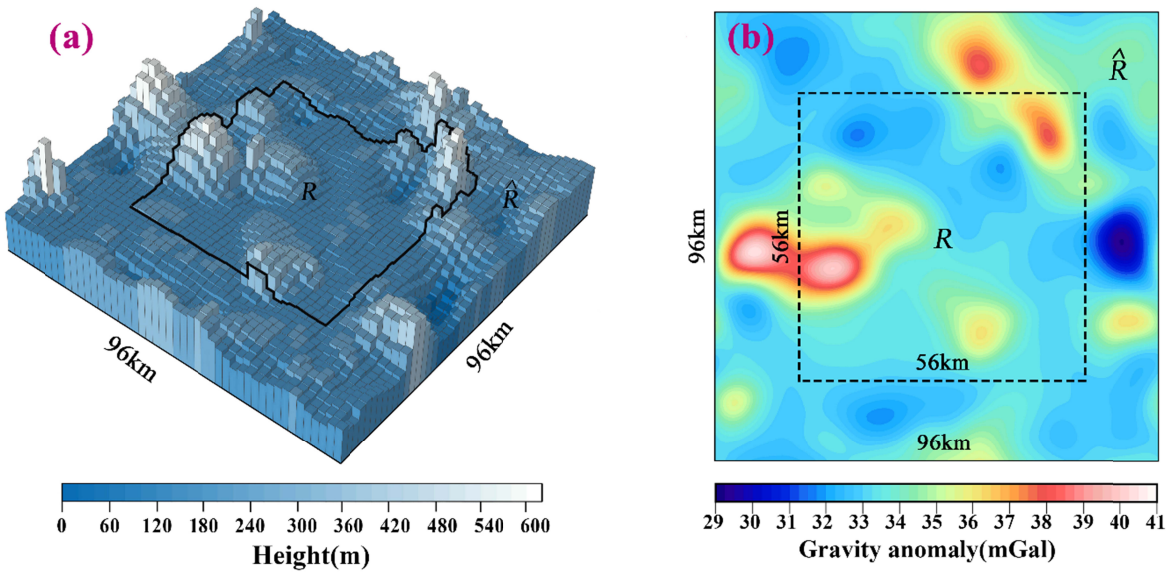

Figure 3. (a) The 2-km step segmentation seafloor topography beneath the region $\hat{R}$, where the topographic fluctuation is obtained from the GEBCO_22 bathymetry model. (b) The distribution of the gravity anomaly on the sea surface generated by this topography when H=6 km.

3.2 Selection of regularization factors

First, the maximum depth is chosen as H=6 km. For the different regularization parameter α (unit: $10^{-18}\mathrm{s}^{-4}\mathrm{m}^{-2}$), the seafloor topography beneath R is solved using **Eq. (20)** without any error in $\delta g_{\hat{R}}$ and with a random error of 1 mGal in $\delta g_{\hat{R}}$, respectively. Subsequently, compared to the real topography, the root mean square (RMS) error can be computed (**Fig. 4a**). **Fig. 4a** shows that the regularization factor α can be appropriately small if there is no error in $\delta g_{\hat{R}}$ on R. For example, when $\alpha = 10^{-5}$, the solved seafloor topography has an error of less than 1.0 m, which is caused by the boundary effect. Additionally, if error exists in $\delta g_{\hat{R}}$ on R, the value of α cannot be too small; the reason for this is that the anti-error property of matrix $A_k^T A_k$ is poor. Notably, the eigenvalues of $A_k^T A_k$ corresponding to the sea depths below the boundary region can easily be disturbed,

which can lead to a large error in the sea depths below the boundary region, and thus affect the accuracy of the bathymetry below R. Therefore, the selection of the regularization factor α must consider the case of error in the gravity anomaly $\delta g_{\hat{R}}$. **Fig. 4a** shows that the optimal value of α should be between 0.1 and 1.0 in the case of maximum depth H=6 km. Simultaneously, the optimal value of α varies with the depth H. Generally, the larger the depth H, the smaller is the optimal value of α.

Fig. 4b shows the RMS error distributions of the solved seafloor topography beneath R for different maximum depths H in the cases of no error and a random error of 1 mGal in $\delta g_{\hat{R}}$, respectively, where $\alpha = 1$ is fixed. According to the examination rule for accuracy, the error ratio (i.e., ratio of error to the average sea depth) can usually be used as an index. For example, as the topographic relief is 610.0 m, the average sea depth is approximately 4695.0 m when H=5 km and the RMS error is about 40.0 m (yellow curve in **Fig. 4b**); thus, the error ratio is 0.85%. **Fig. 4b** shows that that all the error ratios are less than 1%; thus, choosing the regularization factor $\alpha = 1$ is appropriate.

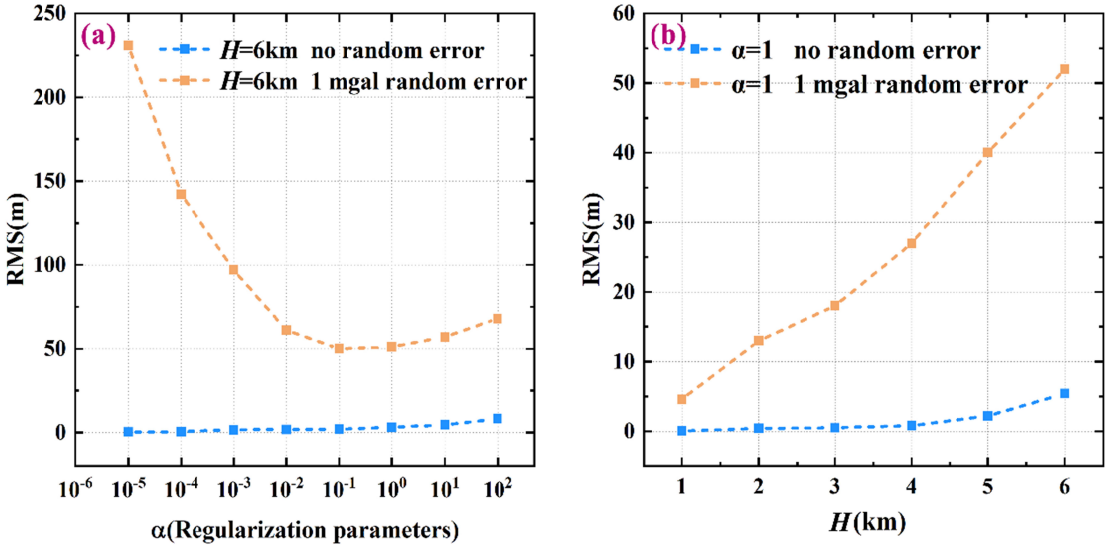

289 **Figure 4.** (a) RMS errors of the prediction results corresponding to different α values for H = 6
290 km. The orange and blue dotted lines represent the iterative convergence curves for no error and
291 1 mGal random error, respectively; (b) Prediction results corresponding to different H values
292 after α is fixed to 1.

293 **3.3 Anti-error characteristics of the linearized systems of equations**

294 This paragraph discusses the anti-error characteristics of **Eq. (11)** or **(20)** where $\alpha = 1$ is
295 chosen. As the gravity anomaly on R mainly results from satellite altimetric data, it contains some
296 error. In the following computations, two kinds of errors are added to the gravity anomaly $\delta g_{\hat{R}}$ on
297 R: the one is the systematic error ε and the other is the random error with a mean value of zero and
298 standard deviation δ. Subsequently, the seafloor topography beneath R is solved using **Eq. (20)**.
299 Furthermore, compared to the real seafloor topography beneath R, the RMS errors of the solved
300 seafloor topography can be computed, and their distributions for different maximum depths H are
301 shown in **Figs. 5a** and **5b**, where **Figs. 5a** and **5b** correspond to the systematic and random errors,
302 respectively. **Figs. 5a** and **5b** show that: (i) the systematic error in $\delta g_{\hat{R}}$ has less influence on the
303 solved seafloor topography compared to the random error; and (ii) the anti-error ability
304 continuously weakens with increasing sea depth. This is because the deeper the seafloor, the
305 smoother the gravity it generates on the sea surface, and the lower is its signal-to-noise ratio for the
306 same size of error. For example, for maximum depth H = 6 km, the RMS errors of the simulation
307 results for the systematic and random errors are 177.0 m and 221.0 m, respectively, when errors in
308 $\delta g_{\hat{R}}$ are both 5 mGal, indicating that the systematic error has less influence on predict topography.
309 Additionally, from the statistical results of the random error with an error of 5 mGal in $\delta g_{\hat{R}}$ (**Fig.**
310 **5b**), all the error ratios of the solved bathymetries are less than 4%, which fully satisfies the

general bathymetry specification necessitating error values of up to 6%. This implies that an accuracy of 5 mGal for the gravity anomaly on the sea surface can guarantee the demand for the inversion of seafloor topography.

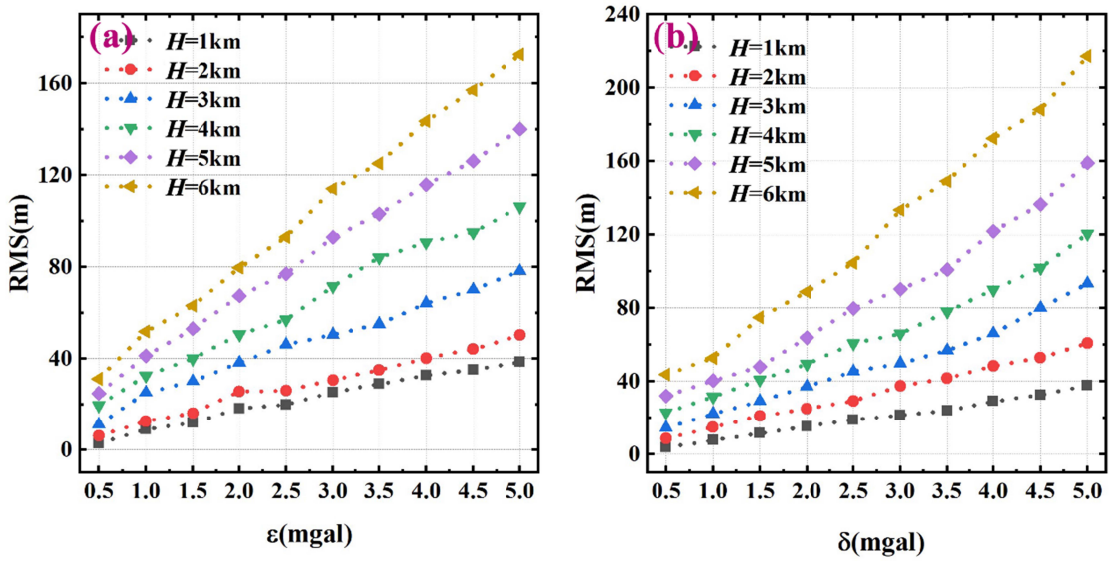

Figure 5. (a) Anti-error curves of the systematic error for different depths. (b) Anti-error curves of random error for different depths.

Meanwhile, to examine the influence of the initial value $h_{ij}^{(0)}$ and the iterative step in solving **Eq. (20)**, the RMS error of the solved seafloor topography using **Eq. (20)** are shown in **Figs. 6a** and **6b**, where no error is added to $\delta g_{\hat{R}}$. **Fig. 6a** shows the RMS error convergence curves for different initial values of $h_{ij}^{(0)}$ in the case of $H = 6$ km; notably, the closer the initial value $h_{ij}^{(0)}$ is to the true value, the faster is the convergence of iterations. **Fig. 6b** shows the relationship between the number of iterations and the RMS error for different maximum sea depths H by considering $h_{ij}^{(0)}$ as 100.0 m. **Fig. 6b** shows that the errors between the solved sea depths and their real values are negligible by solving **Eq. (20)** with 5 to 8 iterations. Overall, we concluded that the sea depth

obtained from the iterative scheme, as expressed in **Eq. (20)**, rapidly converges to its real value for seafloor topographies with different depths.

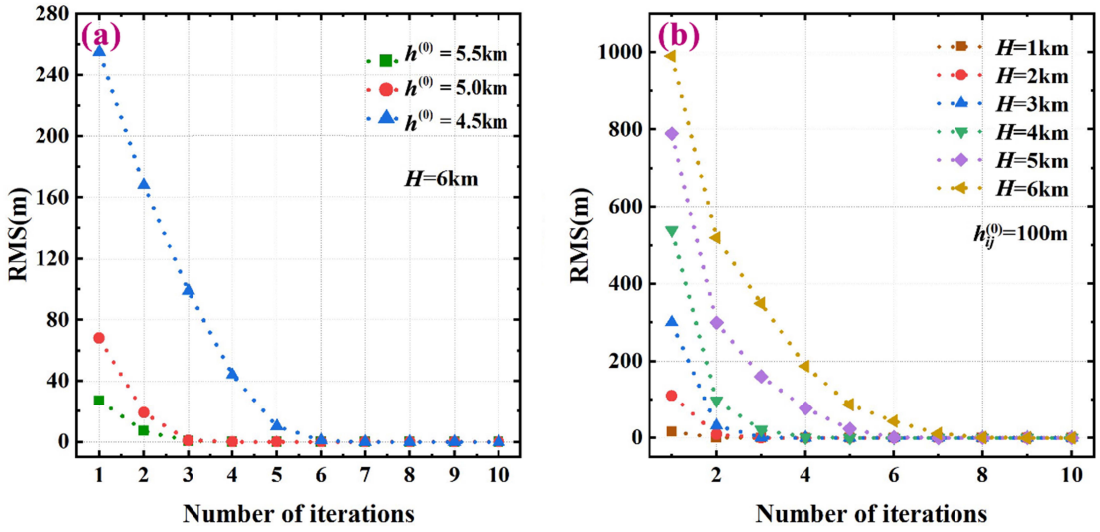

Figure 6. (a) Iterative processes for different initial values when H = 6 km. (b) Iterative processes for different sea depths with a fixed initial value of 100.0 m.

3.4 Assessment for the far effect

To examine the far effect and illustrate how to control it by a piecewise bilinear interpolation on R, the area $\hat{R}$ shown in **Fig. 3a** is extended to a square area of 200 km^2 (**Fig. 7a**) and the area D outside $\hat{R}$ can be referred to as the far region. Furthermore, if the seafloor topography beneath D is also given by the GEBCO_22 bathymetry model, the far effect on R can then be obtained by computing the gravity anomaly generated by the seafloor topography beneath D according maximum depth H. By choosing maximum depth H = 6 km and assuming $\delta g_D(x,y)$ to denote the far effect on R, the difference between $\delta g_D(x,y)$ and $\delta \hat{g}_D(x,y)$ is computed after introducing the piecewise bilinear interpolation function $\delta \hat{g}_D(x,y)$ presented in **Section 2.2.3**. The statistical

results of the difference are shown in **Fig. 7b**. Hence, the error caused by substituting $\delta\hat{g}_D(x,y)$ for $\delta g_D(x,y)$ in **Eq. (14)** is less than 0.3 mGal on average.

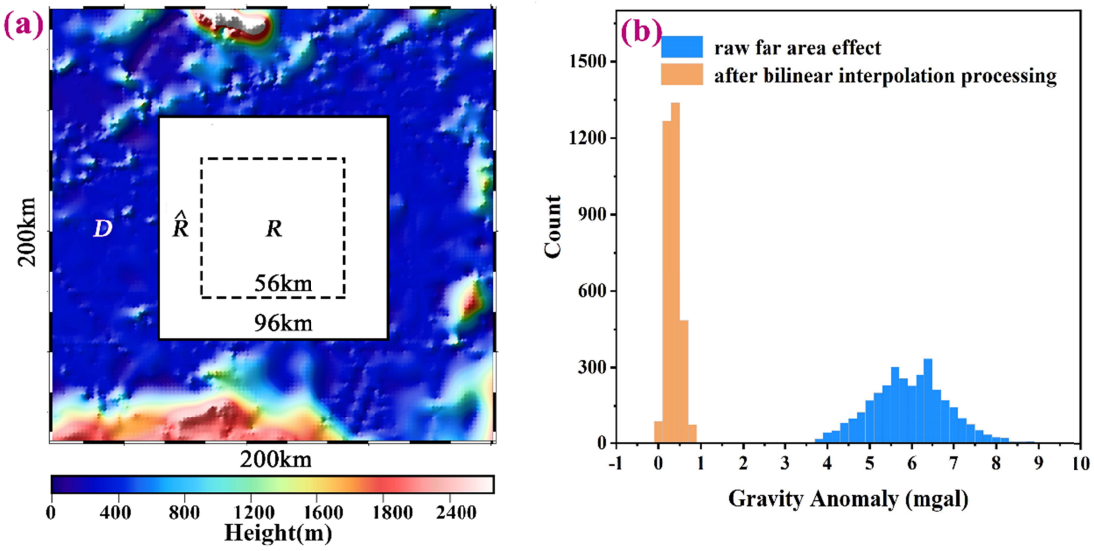

Figure 7. (a) The simulated topography: R, $\hat{R}$ and D represent the corresponding target, boundary and far regions. (b) Histograms of the difference of the far effect and its bilinear interpolation on R, where the orange column indicates the distribution of the influence of the gravity anomaly error caused by the far zone after bidirectional interpolation and the blue column represents the original far zone contribution error distribution.

Additionally, assuming that $\delta\overline{g}_D$ is the average value of $\delta g_D(x,y)$ on R, the statistical results from the "blue curve" shown in **Fig. 7b** indicate that $\delta g_D(x,y)-\delta\overline{g}_D$ can be approximately referred to as the random error with a standard deviation of 0.8 mGal. Therefore, the term $\delta g_D(x,y)$ in **Eq. (14)** can be also replaced by a constant for simple computation. Notably, **Fig. 7b** is created by choosing $M=10$ when introducing $\hat{R}$. Thus, if M is larger, the far effect $\delta g_D(x,y)$ on R is closer to its average value $\delta\overline{g}_D$. However, as the condition $M \le N$ should be satisfied, the choice of $M=10$ is appropriate in this case.

Although the average value $\delta\overline{g}_D$ is approximately equal to the far effect $\delta g_D(x,y)$, the piecewise bilinear interpolation function $\hat{F}(x,y,\mathbf{F})$ is still recommended owing to the presence of another term (i.e., the deep effect) in **Eq. (15)**.

4 Actual Application

4.1 Target region and datasets

A region of the South China Sea at latitudes 13.85°-14.85° N and longitudes 117.25°-118.25° E is selected as the target region *R* and is then divided into four parts as shown in **Fig. 8a**. The underwater topography of each part is solved from the gravity anomaly using **Eq. (20)**, and the whole seafloor topography beneath *R* can be obtained by splicing four parts together. The advantage of such partition is that the boundary effect can be satisfactorily controlled, thereby weakening the complexity in solving the observation equations.

The gravity anomaly used in this paper is chosen from the DTU17 model (**Andersen and Knudsen, 2019**) and has a resolution of 1′×1′ (**Fig. 8a**); its accuracy is roughly between 1.50 and 5.69 mGal in the South China Sea region (Fan et al., 2020). The GEBCO_2022 global topography model published by the International Hydrographic Organization (IHO) is used to evaluate our predicted seafloor topography; its topography under the target region is shown in **Fig. 8b**. Additionally, the data from National Geophysical Data Center (NGDC) with 2512 ship-survey depth points in the target region (**Fig. 8c)** are also used to evaluate our results (www.ngdc.noaa.gov/maps/bathymetry). The GEBCO_2022 global topography model indicates that the maximum and minimum depths in the target region are 4340.0 and 3404.0 m, respectively, and the complexity of the topographic relief is high (**Fig. 8b**); thus, it is appropriate to choose such seafloor topography as the target object.

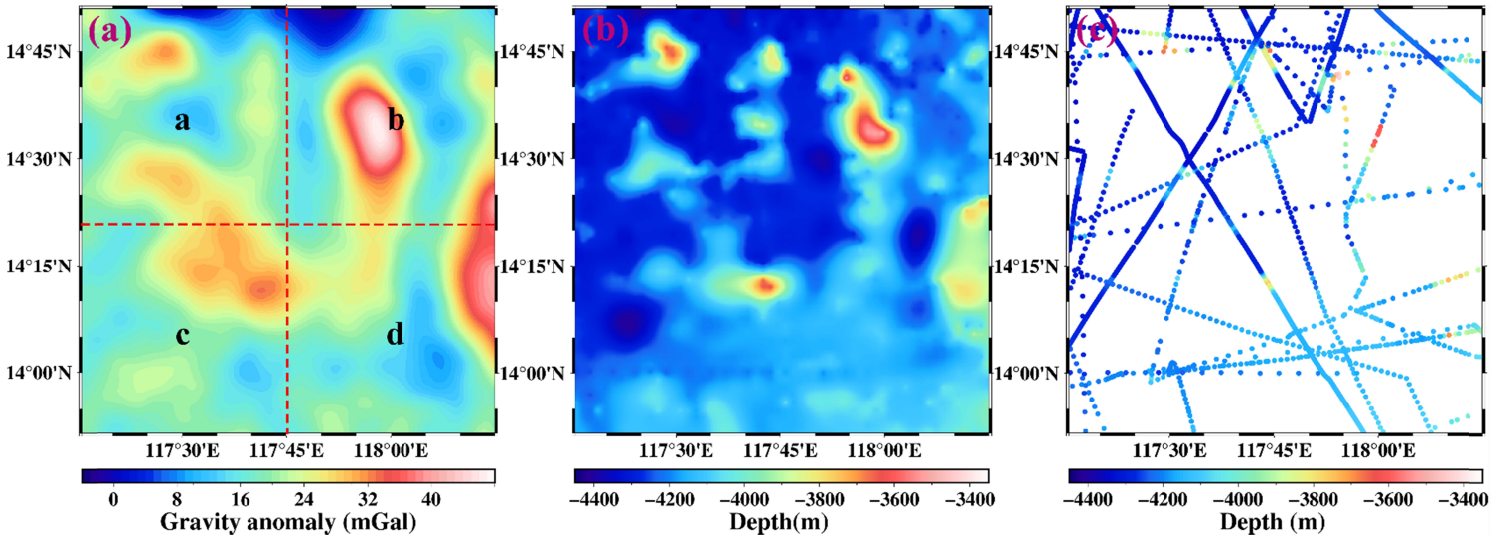

Figure 8. (a) The distribution of gravity anomaly from the DTU17 model in the target region and its spatial resolution is **1′×1′**, where the red dashed line illustrates the zoning so that the areas **a**, **b**, **c** and **d** are equally divided. (b) The bathymetry from the GEBCO_2022 model in the target region. (c) The distribution of the ship soundings data downloaded from the NGDC in the target region.

4.2 Results and comparisons

Based on the algorithm presented in **Section 3**, the prediction topography is shown in **Fig. 9**, where the regularization parameter $\alpha = 1$, the density difference $\Delta\rho = -1.67 \times 10^3 \mathrm{kg/m}^3$, and the extension step width $M = 10$ for $\hat{R}$. The comparison between **Figs. 9a** and **8a** shows a certain similarity between the gravity anomaly and sea depth, which may indicate the suitability of the GGM method to invert the seafloor topography.

Now, we analyze the accuracy of the prediction topography. First, compared with the GEBCO_2022 model, the RMS errors of the solved seafloor topographies are listed in the last column of **Tab. 1**. Second, compared with the NGDC ship-surveyed depths (**Fig. 8c**), the error distributions are shown in **Fig. 9b** and the main statistical indexes of our result are presented in

other columns in **Tab. 1**. As the NGDC data is from the ship survey, they are considered as accurate data. The RMS error of our result to the NGDC data is 127.4 m. Hence, the solved topography is acceptable as ship-survey data are not used in our result.

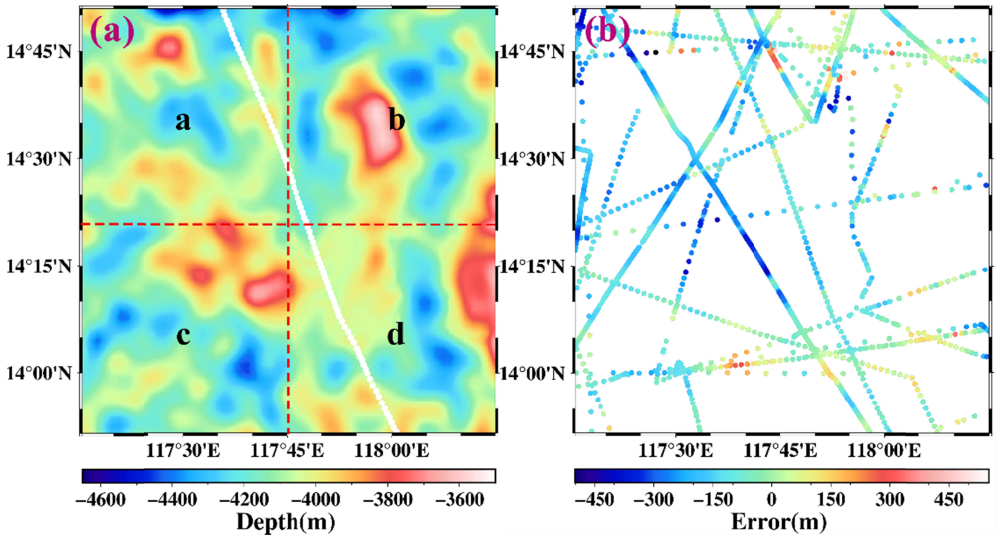

Figure 9. (a) The prediction topography by the analytic iterative algorithm; the white points are HU939013 ship measurements for subsequent error comparison experiments. (b) The error distribution of the prediction results compared with the ship soundings.

Table. 1. Main statistical results of the predicted seafloor topography with known data (unit: m).

Main Indicators	Max depth	Min depth	Mean depth	Max Abs error	Sys error	RMS error	Relative error	Model error
Sub-area a	4590.9	3698.2	4063.6	480.4	25.2	140.6	3.45%	148.0
Sub-area b	4531.4	3570.1	4018.3	533.9	17.9	116.8	2.91%	134.3
Sub-area c	4484.8	3608.3	4011.5	437.5	22.9	144.4	3.59%	153.4
Sub-area d	4473.0	3596.3	4007.6	426.5	13.1	107.8	2.68%	110.8
Region *R*	4590.9	3570.1	4025.3	533.9	19.8	127.4	3.16%	136.9

In this paragraph, a survey line numbered HU939013 (white dashed points in **Fig. 9a**) in the NGDC data is compared with our result. **Fig. 10a** shows the comparison between the gravity anomaly of DTU17 and that along the survey line obtained by forward computation from our predicted seafloor topography, where the maximum absolute, average and RMS differences are 5.3 mGal, 0.4 mGal, and 2.2 mGal, respectively. **Fig. 10b** shows the comparison of the sea depths, where the maximum absolute, average, and RMS errors of depths along the survey line are 146.3 m, 14.9 m, and 73.42 m. **Fig. 5b** shows the anti-error analysis results; when the maximum depth is 5 km and the random error is 2.5 mGal, the RMS error of the simulation result is 79.0 m. The RMS error of the gravity anomaly difference along the survey line is 2.2 mGal, and the corresponding RMS error for the prediction depth is 73.4 m. This indicates that the numerical simulation results can reflect the final prediction accuracy to a certain extent.

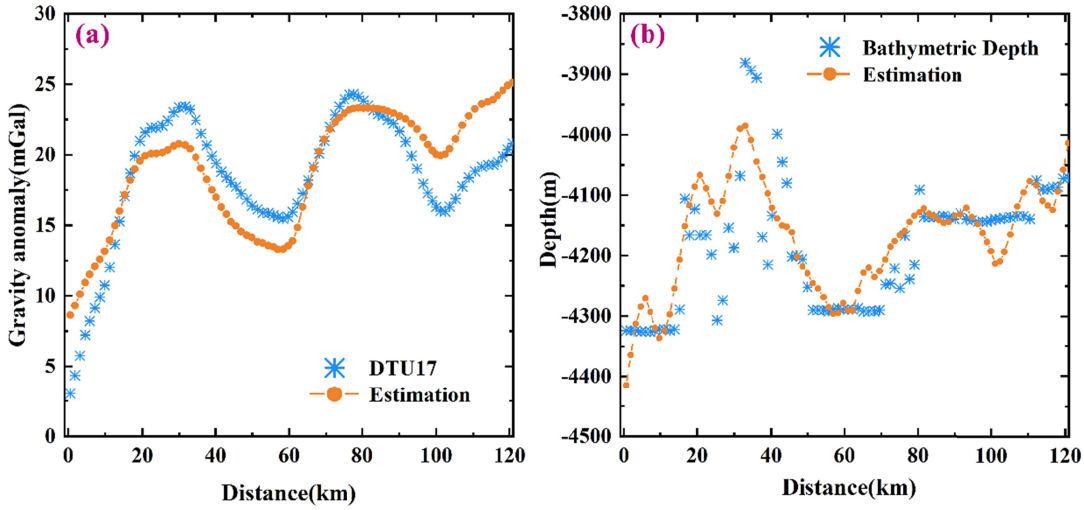

412 **Figure 10.** (a) Comparison between the gravity anomaly of the DTU17 and that obtained in our
413 result by forward computation along the line labeled HU939013. (b) Comparison between
414 ship-survey depths and our predicted depths along the line labeled HU939013.

415 Notably, the known bathymetry data must first be applied to examine the accuracy of the
416 predicted seafloor topography. However, for a certain region on the sea surface, the bathymetry
417 data is mainly obtained along the ship route; thus, its distribution may be relatively sparse in the
418 region. Therefore, using only the bathymetry data as a standard in examining the accuracy of
419 seafloor topography is not comprehensive. Notably, **Eq. (8)** indicated the relationship between
420 the sea depth and gravity anomaly on the sea surface; thus, the gravity anomaly on the sea
421 surface can also be used as an auxiliary standard to evaluate the accuracy of the seafloor
422 topography. **Dixon et al. (1983)** verified that the part of gravity anomaly with wavelengths larger
423 than 30 km is mainly controlled by the far topography, and only the high frequency part with
424 wavelengths less than 30 km can be used to examine accuracy of the seafloor topography.

425 Now, the gravity anomalies on the target region *R* can be obtained by forward computations
426 for the solved seafloor topography and the corresponding GEBCO_ 22 topography model
427 respectively, and their RMS differences to the DTU17 gravity anomaly are computed after
428 subtracting the DTU17 gravity anomaly and filtering out the low-frequency parts with
429 wavelengths larger than 30 km (**Luis, 2006**). Notably, such RMS differences can be considered
430 as a match degree with respect to the DTU17, namely, the smaller the RMS difference, the better
431 the matching of the seafloor topography with DTU17. By computations, the RMS differences to
432 the DTU17 on *R* for the solved topography and GEBCO_22 model are 1.0 mGal and 1.8 mGal
433 respectively, which implies that our result is a better match with the DTU 17 gravity field model

than that obtained by the GEBCO-22 bathymetry model. Therefore, the solved topography is better than one from the GEBCO-22 bathymetry model on *R* to some extent.

Finally, we indicate that the seafloor topography solved in this paper only uses the gravity anomaly on the target region *R*, and does not employ any known ship survey data. Additionally, the measured sea depth data along the ship route can be regarded as a local index to examine the seafloor topography, whereas the matching degree with the gravity anomaly can be regarded as an overall index in the target region.

5 Discussion and Conclusions

In this paper, the grid step length is 2 km, implying that the topography undulations within an area of 2 km×2 km are represented by the average depth, which means that the topography undulations within 2 km×2 km cannot be identified (**Xu and Yu, 2022**). Hopefully, the next generation of Surface Water and Ocean Topography (SWOT) satellites may revolutionize the improvement of marine gravity anomalies with a spatial resolution of 1 km (**Bouman et al., 2011; Morrow et al., 2019; Yu J H et al., 2021**). This may significantly improve the prediction accuracy of seafloor topography. In all, it is important for improving the accuracy of topography prediction to obtain gravity data with higher resolutions and higher accuracies.

The advantages of the analytical iterative method established in this paper are as follows: first, we directly utilize the original gravity anomaly data without filtering or separating the long/short-waves; second, it is not required to introduce the isostatic response function with empirical parameters. The only prerequisite is to weaken the influence of the boundary and far region effects to solve the equations together, which can simplify the calculation.

In summary, we develop a new analytical iterative method to predict topography by building a set of observation equations using the gravity anomaly. Based on numerical simulation experiments, we analyze the accuracy of the prediction results by refining the error sources and investigating the corresponding error weakening methods. In all, the main research results of this paper can be summarized as follows: first, based on the gravity expression of a single rectangular prism, we establish a system of observation equations between the topography and gravity anomaly, and the solvability of the equations is verified by numerical simulation. Second, the disturbance elements are mainly divided as the boundary, far and deep effects, and the regularization algorithm and piecewise bilinear interpolation function are used to process the disturbance factors, respectively. Third, the algorithm proposed in this paper is applied to the actual sea area, and the ship soundings are used to verify the accuracy of the prediction results. The RMS error of the prediction topography reaches 127.4 m in the sea region with an average depth of 4025.3 m, and the relative accuracy of the prediction reached 3.16%.

Acknowledgments

This study is funded by the National Nature Science Funds of China (No:42274010 and No: 41774089)

Data Availability Statement

The single-beam data are provided by National Oceanic and Atmospheric Administration (NOAA) https://www.ncei.noaa.gov/maps/bathymetry/. The GEBCO_2022 can be downloaded from https://www.gebco.net/data_and_products/historical_data_sets/. The DTU17 is available from https://ftp.space.dtu.dk/pub/DTU17/1_MIN/.

Conflict of Interest:

The authors declare no conflict of interest

References

Abulaitijiang, A., Andersen, O. B., & Sandwell, D. (2019). Improved Arctic Ocean Bathymetry Derived From DTU17 Gravity Model. *Earth and Space Science*, *6*(8), 1336–1347. https://doi.org/10.1029/2018EA000502

Andersen, O. B., & Knudsen, P. (2019). The DTU17 Global Marine Gravity Field: First Validation Results. In S. P. Mertikas, & R. Pail (Eds.), *Fiducial Reference Measurements for Altimetry (83-87)*. https://doi.org/10.1007/1345_2019_65

Baudry, N., & Calmant, S. (1996). Seafloor mapping from high-density satellite altimetry. *Marine Geophysical Researches, 18(2–4),* 135–146.https://doi.org/10.1007/bf00286074.

Baudry, N., Diament, M., & Albouy, Y. (1987). Precise location of unsurveyed seamounts in the Austral archipelago area using SEASAT data. *Geophysical Journal of the Royal Astronomical Society, 89(3)*, 869–888. https://doi.org/10.1111/j.1365-246x.1987.tb05199.x.

Becker, J. J., Sandwell, D. T., Smith, W. H. F., Braud, J., Binder, B., Depner, J., et al. (2009). Global bathymetry and elevation data at 30 arcseconds resolution: SRTM30_PLUS. *Marine Geodesy, 32(4),* 355–371. https://doi.org/10.1080/01490410903297766

Blakely, R. J. (1995). Potential Theory in Gravity & Magnetic Applications. Potential theory in gravity and magnetic applications. by Blakely, R. J., *Cambridge University Press, Cambridge (UK)*, 1995, XIX + 441 p. ISBN 0-521-41508-X.

Bouman, J., Bosch, W., & Sebera, J. (2011). Assessment of systematic errors in the computation of gravity gradients from satellite altimeter data.*Marine Geodesy, 34(2),* 85–107. https://doi.org/10.1080/01490419.2010.518498

Caballero, I, Richard, P. S. (2020). Towards Routine Mapping of Shallow Bathymetry in Environments with Variable Turbidity: Contribution of Sentinel-2A/B Satellites Mission. *Remote Sensing, 12(3)*: 451–. https://doi.org/10.3390/rs12030451

Calmant, S. (1994). Seamount topography by least-squares inversion of altimetric geoid heights and shipborne profiles of bathymetry and/or gravity anomalies. *Geophysical Journal International, 119(2),* 428–452. https://doi.org/10.1111/j.1365-246x.1994.tb00133.x

Calmant, S., Baudry, N. (1996). Modelling bathymetry by inverting satellite altimetry data: A review. *Marine Geophysical Researches, 18(2–4)*,123–134. https://doi.org/10.1007/bf00286073

Dixon, T. H., Naraghi, M., McNutt, M. K., & Smith, S. M. (1983). Bathymetric prediction from Seasat altimeter data. *Journal of Geophysical Research, 88(C3),* 1563–1571. https://doi.org/10.1029/jc088ic03p01563

Fan, D., Li, S., Meng, S., Lin, Y., Xing, Z., Zhang, C., et al. (2020). Applying Iterative Method to Solving High-Order Terms of Seafloor Topography. *Marine Geodesy*, *43*(1), 63–85. https://doi.org/10.1080/01490419.2019.1670298

Fan, D., Li, S., Li, X., Yang, J., Wan, X Y. (2021). Seafloor Topography Estimation from Gravity Anomaly and Vertical Gravity Gradient Using Nonlinear Iterative Least Square Method[J]. *Remote Sensing., 13(1)*, 64; https://doi.org/10.3390/rs13010064

Heiskanen, W., Moritz, H. (1967). *Physical Geodesy*. Freeman W H, San Francisco

Hsiao, Y. S., Kim, K., Kim, J. W., Lee, B. Y., & Hwang, C. (2011). Bathymetry estimation using the gravity-geologic method: An investigation of density contrast predicted by the downward continuation method. *Terrestrial, Atmospheric and Oceanic Sciences, 22(3)*, 347–358. https://doi.org/10.3319/tao.2010.10.13.01(oc)

Hu M Z, Li J C, Li H, Xin L. (2014). Bathymetry predicted from vertical gravity gradient anomalies and ship soundings. *Geodesy and Geodynamics,* 5: 41–46

Hwang, C. (1999). A bathymetric model for the South China sea from satellite altimetry and depth data. *Marine Geodesy,* 22(1), 37–51. https://doi.org/10.1080/014904199273597

Ibrahim, A., & Hinze, W. J. (1972). Mapping buried bedrock topography with gravity. Ground Water, 10(3), 18–23. https://doi.org/10.1111/j.1745-6584.1972.tb02921.

Jekeli C. (2017). *Spectral methods in geodesy and geophysics. Boca Raton*, FL: CRC Press.

Kim J W., Frese R., Lee B Y., Roman D R., Doh S. (2011). Altimetry-derived gravity predictions of bathymetry by gravity-geologic method. *Pure and Applied Geophysics, 168(5)*, 815–826. https://doi.org/10.1007/s00024-010-0170-5

529 Kim S., Wessel P. (2016). New analytic solutions for modeling vertical gravity gradient anomalies. *Geochemistry,*
530 *Geophysics, Geosystems,17(5),* 1915–1924. https://doi.org/10.1002/2016gc006263
531 Luis J F, Neves M C. (2006). The isostatic compensation of the Azores Plateau: A 3D admittance and coherence
532 analysis[J]. *Journal of Volcanology & Geothermal Research, 156(1-2)*:10-22.
533 Lyzenga D R. (1978). Passive remote sensing techniques for mapping water depth and bottom features. *Applied*
534 *Optics, 17(3):* 379–383.
535 Nagy D. (1966). The gravitational attraction of a right rectangular prism. Geophysics, v. 31, no. 2, p. 362-371.
536 *Geoarabia Journal of the Middle East Petroleum Geosciences*
537 Nagy D., Papp G., Benedek, J. (2000). The gravitational potential and its derivatives for the prism. *Journal of*
538 *Geodesy, 74(7–8),* 552–560.https://doi.org/10.1007/s001900000116
539 Parker, R. L. (1972). The rapid calculation of potential anomalies. *Geophysical Journal of the Royal Astronomical*
540 *Society, 31(4)*, 447–455.https://doi.org/10.1111/j.1365-246x.1973.tb06513.x
541 Rasheed, S., Warder, S. C., Plancherel, Y., & Piggott, M. D. (2021). An improved gridded bathymetric data set and
542 tidal model for the Maldives archipelago. *Earth and Space Science, 8,* e2020EA001207.
543 https://doi.org/10.1029/2020EA001207
544 Sandwell, D. T., & Smith, W. H. F. (1997). Marine gravity anomaly from Geosat and ERS 1 satellite altimetry.
545 *Journal of Geophysical Research,105(B5),* 10039–10054. https://doi.org/10.1029/96jb03223
546 Sandwell, D. T., Müller, R. D., Smith, W. H. F., Garcia, E., & Francis, R. (2014). New global marine gravity model
547 from CryoSat-2 and Jason-1 reveals buried tectonic structure. *Science, 346(6205),* 65–67.
548 https://doi.org/10.1126/science.1258213
549 Sandwell, D. T., Smith, W. H. F., Gille, S., Kappel, E., Jayne, S., Soofi, K., et al. (2006). Bathymetry from space:
550 Rationale and requirements for a new high-resolution altimetric mission. *Comptes Rendus Geoscience,*
551 *338(14–15),* 1049–1062. https://doi.org/10.1016/j.crte.2006.05.014
552 Smith, W. H. F., Sandwell, D. T. (1997). Global sea floor topography from satellite altimetry and ship depth
553 soundings. *Science, 277(22)*,1956–1962. https://doi.org/10.1126/science.277.5334.1956
554 Stumpf R P, Kristine H, Mark S .(2003). Determination of water depth with high-resolution satellite imagery over
555 variable bottom types. *Limnology and Oceanography,* 48(1part2): 547–556.

556 Xu, H., Yu, J.H. (2022). Using an iterative algorithm to predict topography from vertical gravity gradients and ship
557 soundings. *Earth and Space Science,* 9, e2022EA002437. https://doi. org/10.1029/2022EA00243
558 Yang, J. J., Jekeli, C., & Liu, L. (2018). Seafloor topography estimation from gravity gradients using simulated
559 annealing. *Journal of Geophysical Research,* 123, 6958–6975.
560 Yu, J. H., Xu, H., & Wan, X. Y. (2021). An analytical method to invert the seabed depth from the vertical
561 gravitational gradient*. Marine Geodesy,44(4),* 306–326. https://doi.org/10.1080/01490419.2021.1905756
562 Yu, D. C, Hwang C, Andersen O. B, Chang E. T. Y, Gaultier L. (2021). Gravity recovery from SWOT altimetry
563 using geoid height and geoid gradient. Remote Sensing of Environment, 265(2021):112650.
564 DOI:10.1016/j.rse.2021.112650.
565 Zhu, L. Z. (2007). *Gradient modeling with gravity and GEM.* OSU report.

566

Figure.

Sea surface gravity anomaly information and distribution

Gravity anomaly data in the image is from DTU17, and the digital elevation model is from GEBCO22.These data are only used for painting

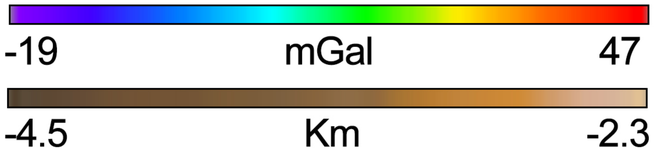

Cross section of the Earth

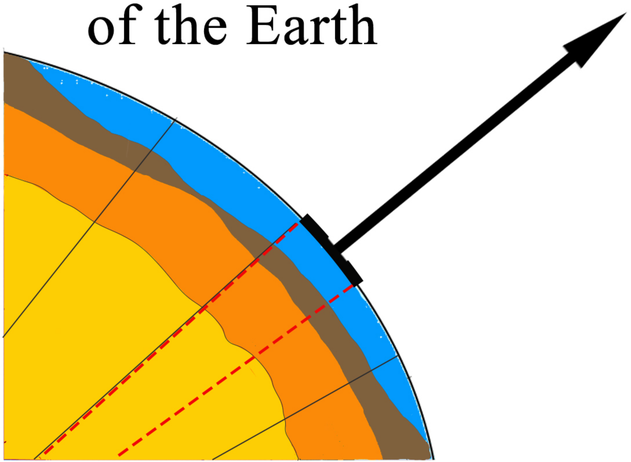

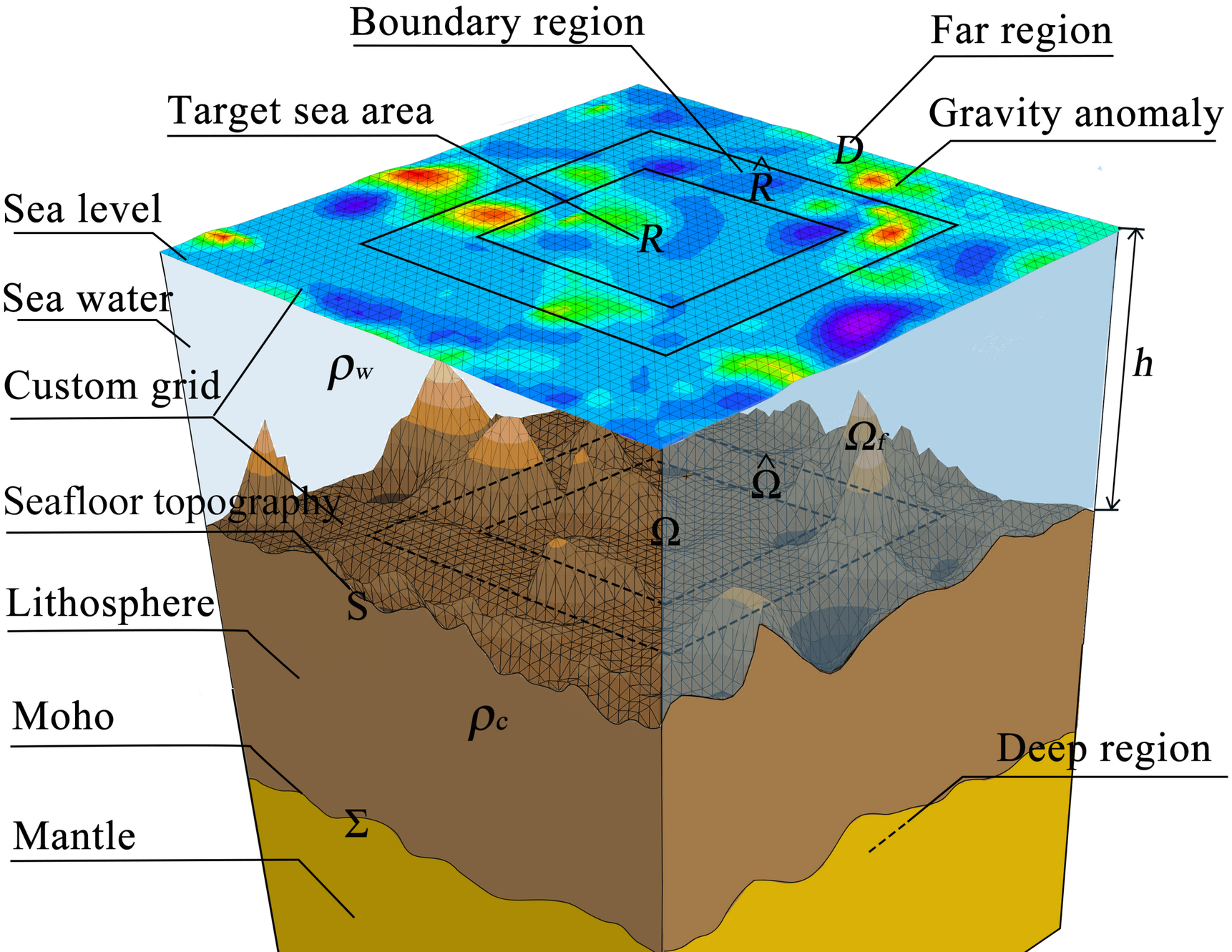

Figure.

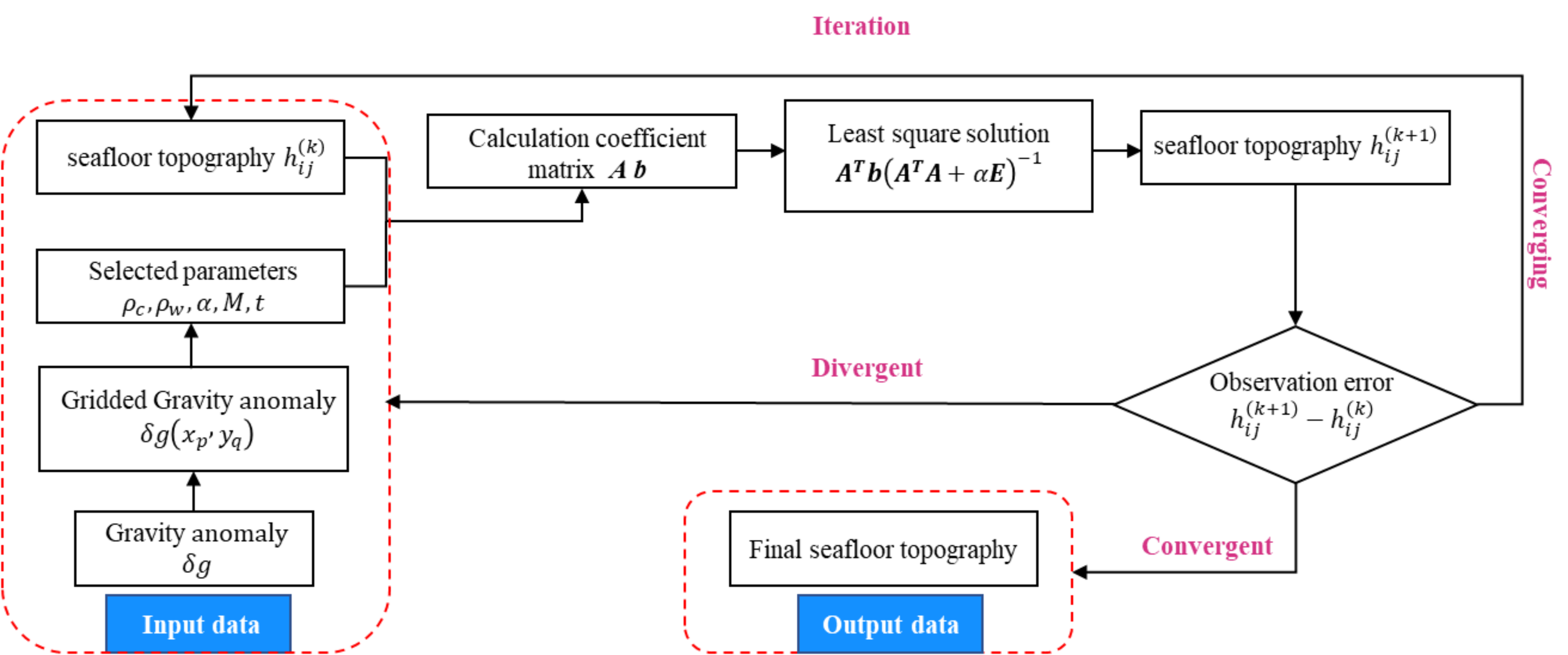
Iteration
seafloor topography $h_{ij}^{(k)}$
Calculation coefficient matrix $\boldsymbol{A}\ \boldsymbol{b}$
Least square solution $\boldsymbol{A^T b}\left(\boldsymbol{A^T A}+\alpha \boldsymbol{E}\right)^{-1}$
seafloor topography $h_{ij}^{(k+1)}$
Converging
Selected parameters $\rho_c, \rho_w, \alpha, M, t$
Divergent
Gridded Gravity anomaly $\delta g(x_p, y_q)$
Observation error $h_{ij}^{(k+1)} - h_{ij}^{(k)}$
Gravity anomaly δg
Convergent
Final seafloor topography
Input data
Output data

Figure.

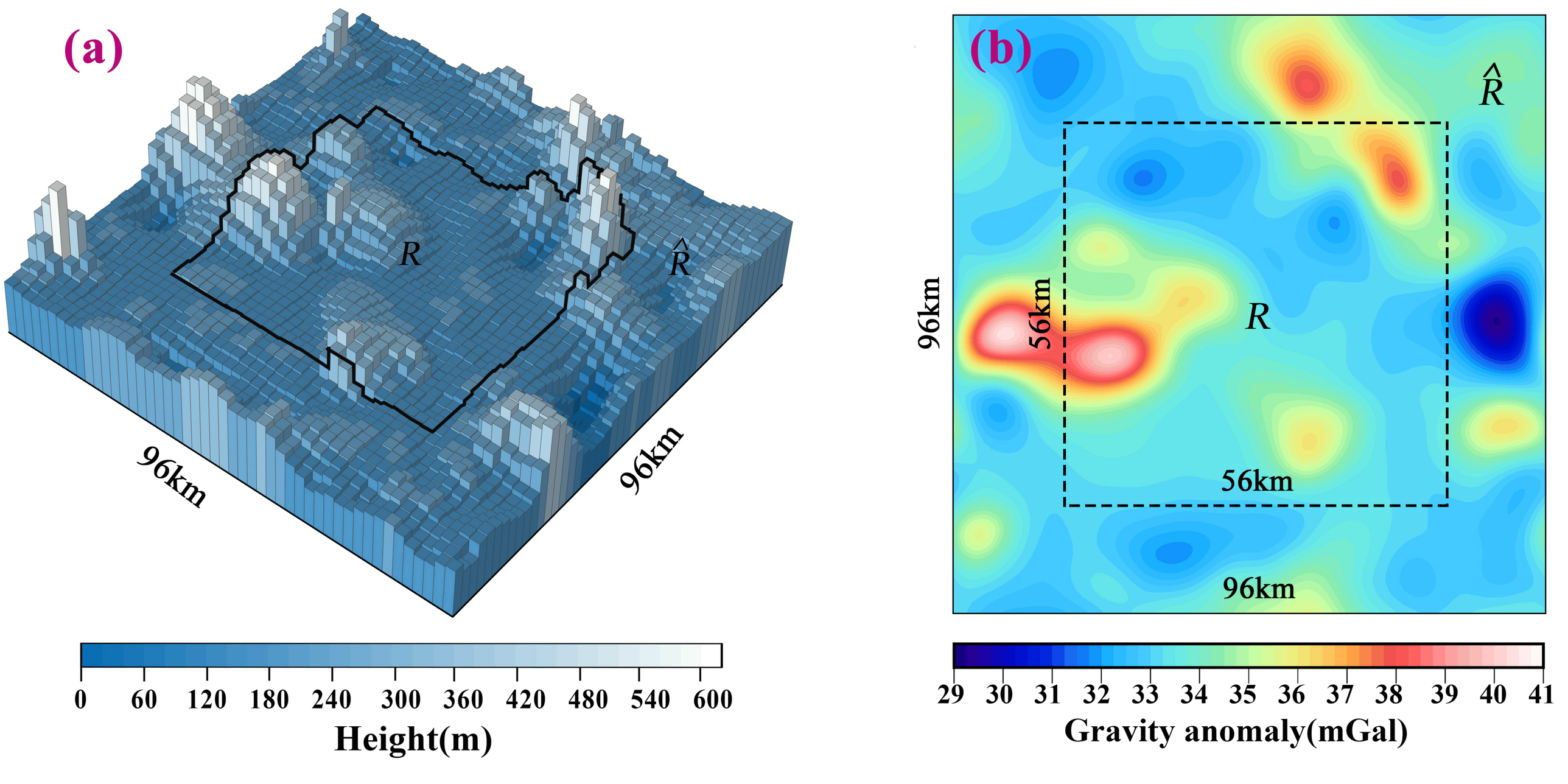
(a)
R
$\hat{R}$
96km
96km
0
60
120
180
240
300
360
420
480
540
600
Height(m)
(b)
$\hat{R}$
96km
56km
R
56km
96km
29
30
31
32
33
34
35
36
37
38
39
40
41
Gravity anomaly(mGal)

Figure.

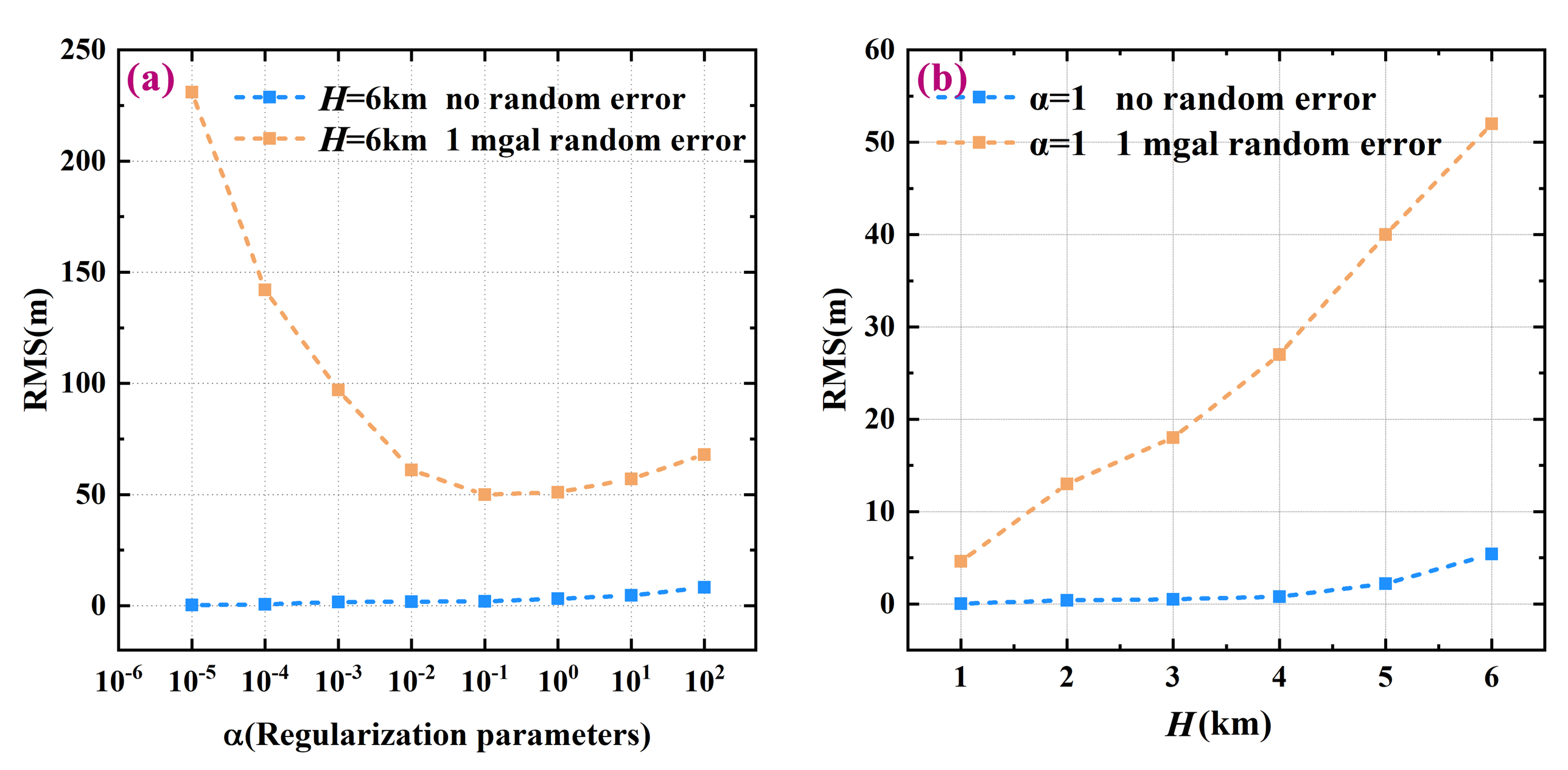
(a)
H=6km no random error
H=6km 1 mgal random error
RMS(m)
250
200
150
100
50
0
10-6
10-5
10-4
10-3
10-2
10-1
100
101
102
α(Regularization parameters)
(b)
α=1 no random error
α=1 1 mgal random error
RMS(m)
60
50
40
30
20
10
0
1
2
3
4
5
6
H(km)

Figure.

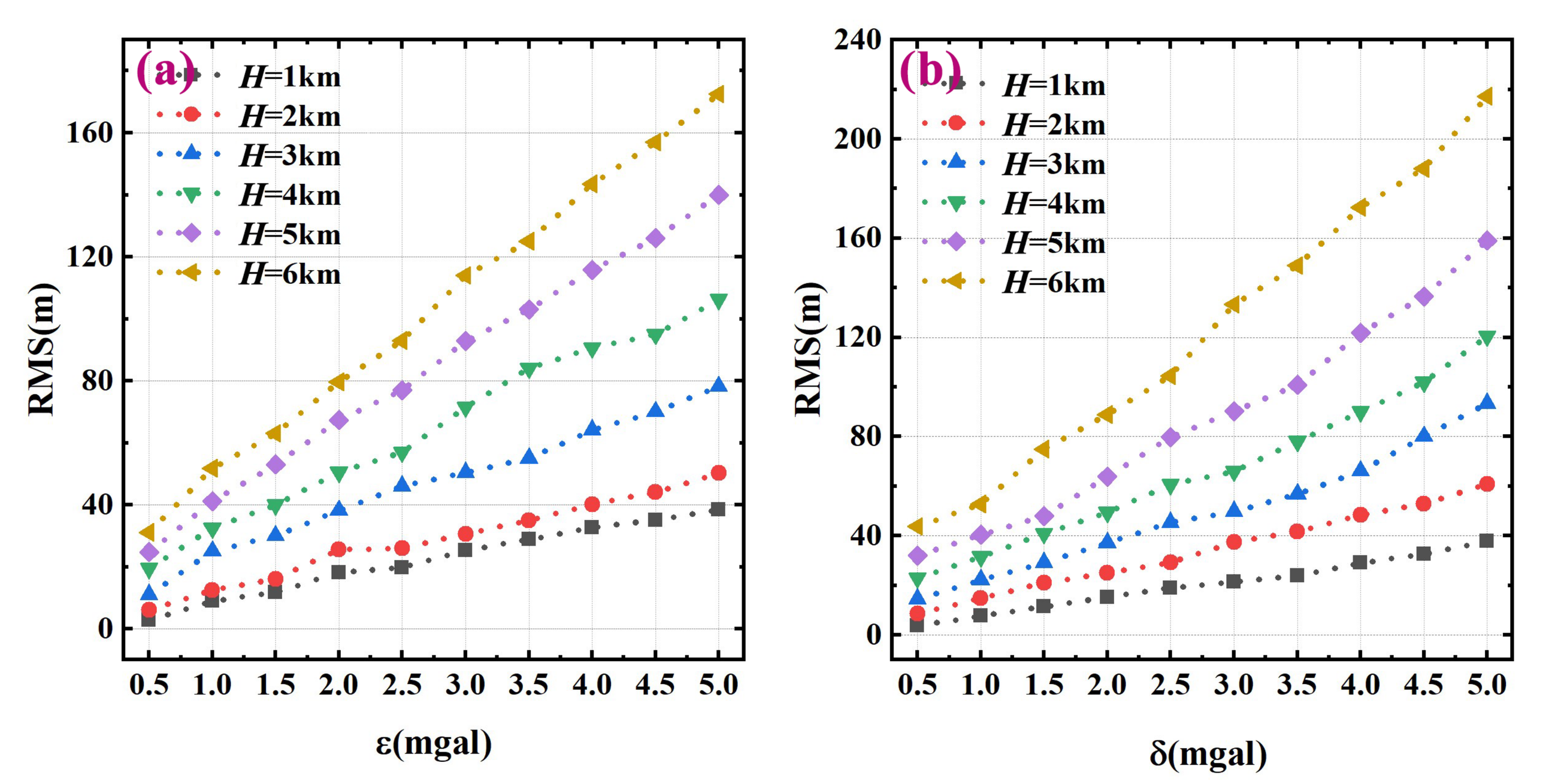
(a)
H=1km
H=2km
H=3km
H=4km
H=5km
H=6km
RMS(m)
0
40
80
120
160
0.5
1.0
1.5
2.0
2.5
3.0
3.5
4.0
4.5
5.0
ε(mgal)
(b)
H=1km
H=2km
H=3km
H=4km
H=5km
H=6km
RMS(m)
0
40
80
120
160
200
240
0.5
1.0
1.5
2.0
2.5
3.0
3.5
4.0
4.5
5.0
δ(mgal)

Figure.

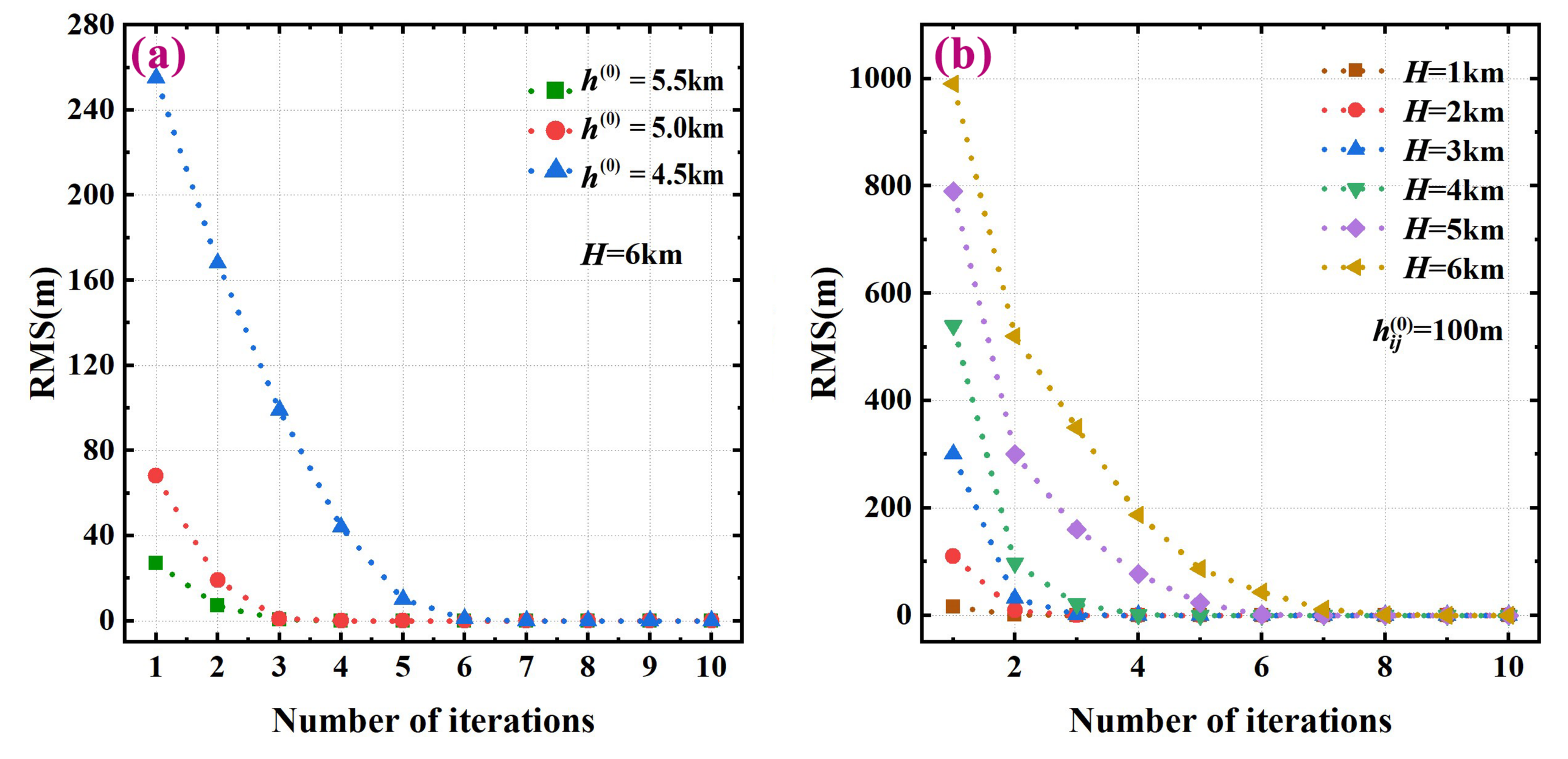
(a)
$h^{(0)}$ = 5.5km
$h^{(0)}$ = 5.0km
$h^{(0)}$ = 4.5km
H=6km
RMS(m)
Number of iterations
(b)
H=1km
H=2km
H=3km
H=4km
H=5km
H=6km
$h_{ij}^{(0)}$=100m
RMS(m)
Number of iterations

Figure.

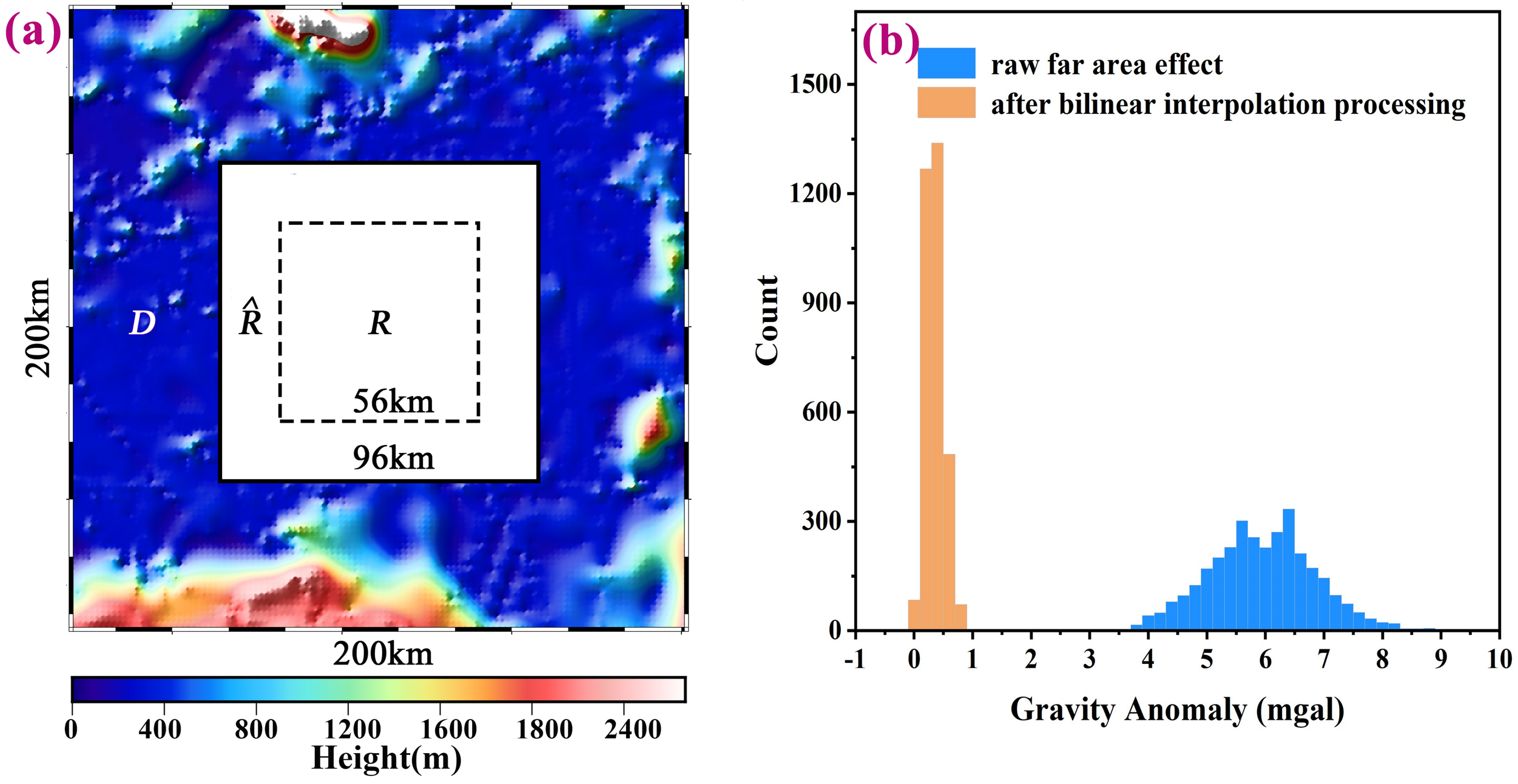
(a)
D
$\hat{R}$
R
56km
96km
200km
200km
0
400
800
1200
1600
1800
2400
Height(m)
(b)
raw far area effect
after bilinear interpolation processing
Count
1500
1200
900
600
300
0
-1
0
1
2
3
4
5
6
7
8
9
10
Gravity Anomaly (mgal)

Figure.

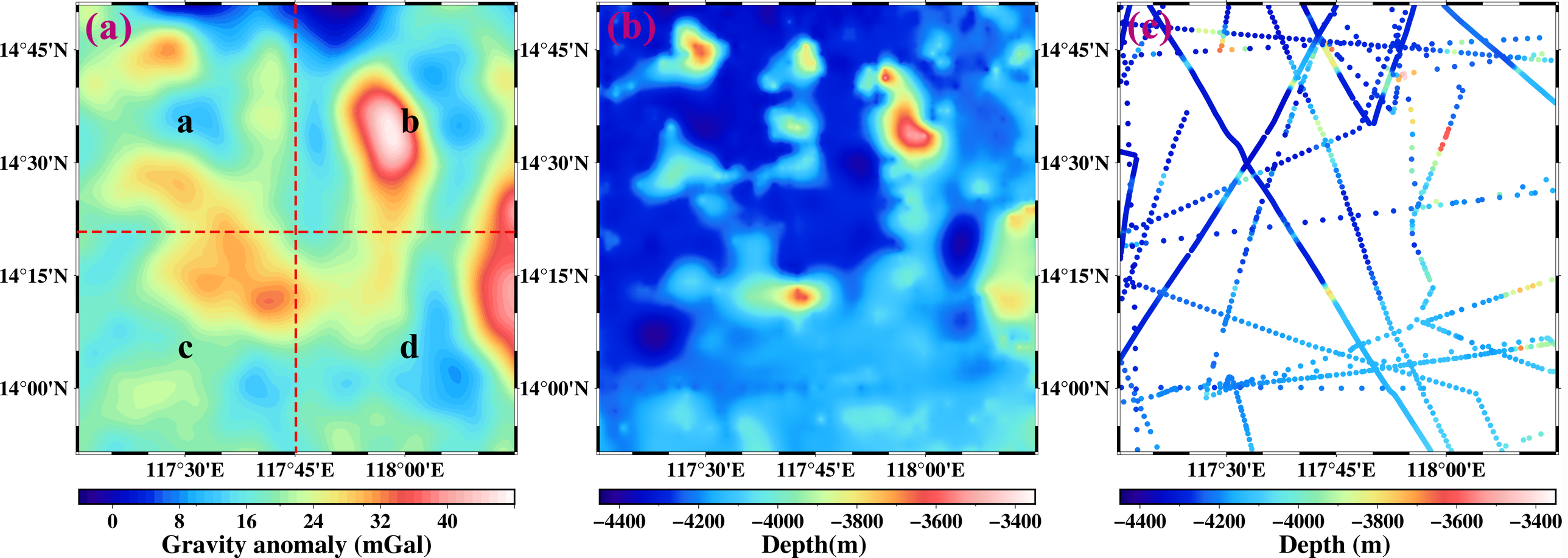
(a)
(b)
(c)
a
b
c
d
14°45'N
14°30'N
14°15'N
14°00'N
117°30'E
117°45'E
118°00'E
0
8
16
24
32
40
Gravity anomaly (mGal)
−4400
−4200
−4000
−3800
−3600
−3400
Depth(m)
Depth (m)

Figure.

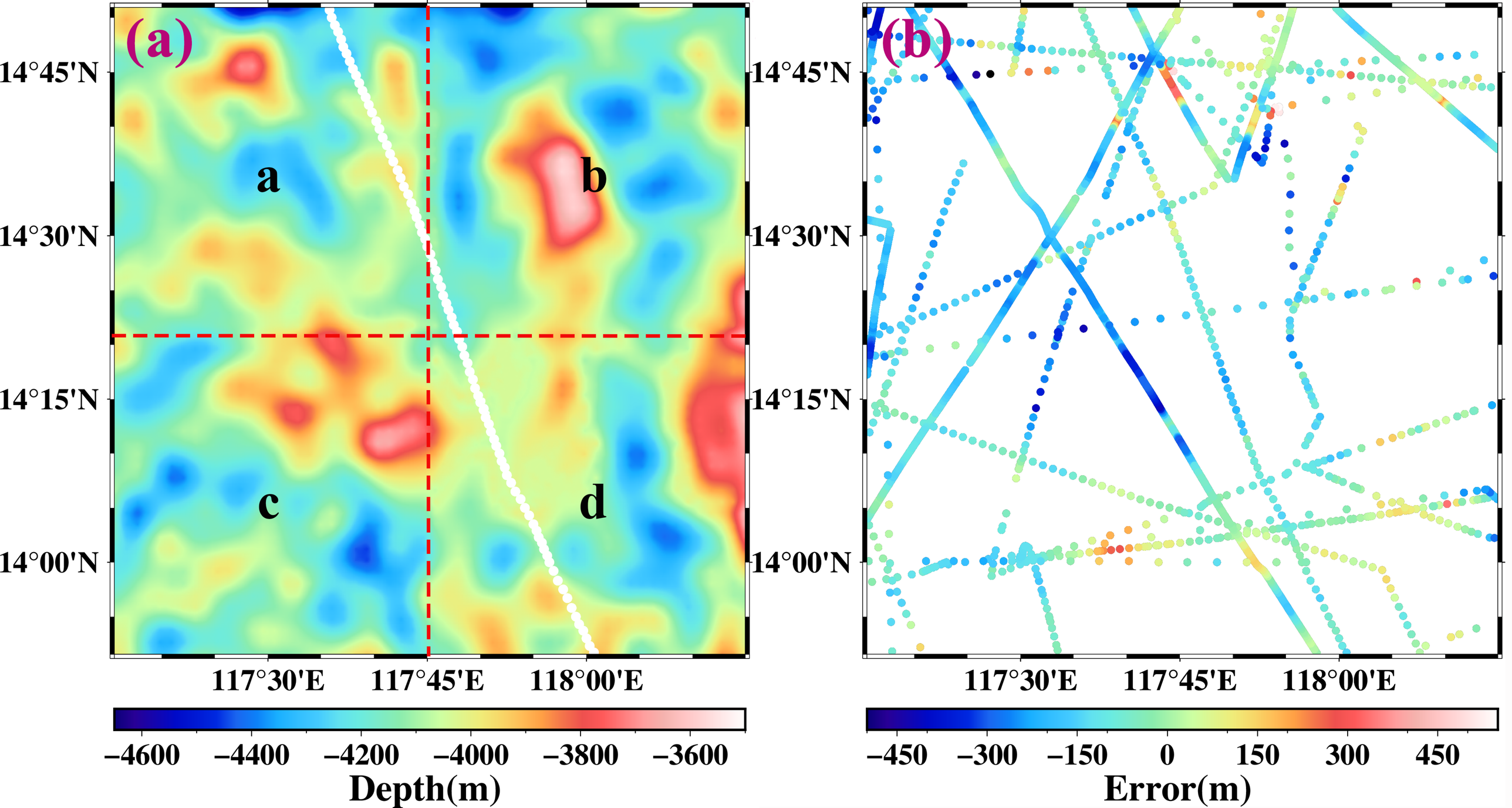
(a)
(b)
a
b
c
d
14°45'N
14°30'N
14°15'N
14°00'N
117°30'E
117°45'E
118°00'E
−4600
−4400
−4200
−4000
−3800
−3600
Depth(m)
−450
−300
−150
0
150
300
450
Error(m)

Figure.

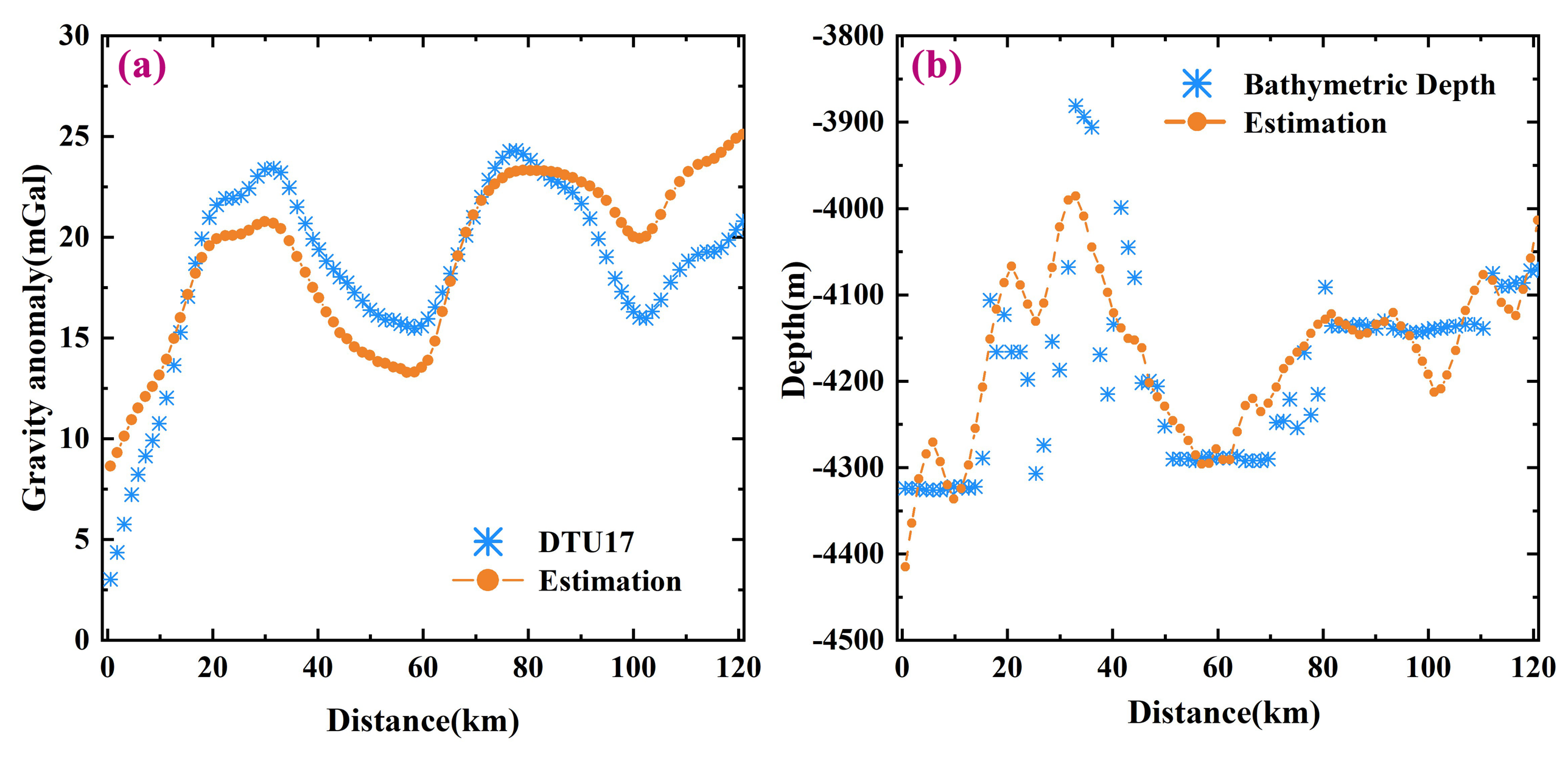
(a)
Gravity anomaly(mGal)
30
25
20
15
10
5
0
0
20
40
60
80
100
120
Distance(km)
DTU17
Estimation
(b)
Depth(m)
-3800
-3900
-4000
-4100
-4200
-4300
-4400
-4500
0
20
40
60
80
100
120
Distance(km)
Bathymetric Depth
Estimation